water

MDPI

Article

Modeling Extreme Water Levels in the Salish Sea: The Importance of Including Remote Sea Level Anomalies for Application in Hydrodynamic Simulations

Eric E. Grossman [1,*], Babak Tehranirad [1], Cornelis M. Nederhoff [2], Sean C. Crosby [1], Andrew W. Stevens [1], Nathan R. Van Arendonk [1], Daniel J. Nowacki [1], Li H. Erikson [1] and Patrick L. Barnard [1]

[1] U.S. Geological Survey, Pacific Coastal and Marine Science Center, Santa Cruz, CA 95060, USA; babak.tehranirad@gmail.com (B.T.); schcrosby@gmail.com (S.C.C.); astevens@usgs.gov (A.W.S.); nathan.vanarendonk@gmail.com (N.R.V.A.); dnowacki@usgs.gov (D.J.N.); lerikson@usgs.gov (L.H.E.); pbarnard@usgs.gov (P.L.B.)

[2] Deltares USA, Silver Spring, MD 20910, USA; kees.nederhoff@deltares-usa.us

* Correspondence: egrossman@usgs.gov

Abstract: Extreme water-level recurrence estimates for a complex estuary using a high-resolution 2D model and a new method for estimating remotely generated sea level anomalies (SLAs) at the model boundary have been developed. The hydrodynamic model accurately resolves the dominant physical processes contributing to extreme water levels across the Washington State waters of the Salish Sea, including the relative contribution of remote SLA and other non-tidal residual processes that drive extreme water levels above the predicted tide. The model's predictions have errors of less than 15 cm (<5% of 3–4 m tidal range) at eight tide gauge locations across the model domain. The influence of remote SLAs at the seaward boundary of the model was implemented using a multivariate regression of readily available and locally relevant wind, sea surface temperature, and pressure anomaly data, combined with El Niño Index data (R^2 = 0.76). The hydrodynamic model simulations using the remote SLA predictor compared well with simulations using the widely used data-assimilative global ocean model HYCOM SLA data (root mean square difference of 5.5 cm). Extreme water-level recurrence estimates with and without remote SLA show that remote forcing accounts for 50–60% of the total water level anomaly observed along Salish Sea shorelines. The resulting model simulations across decadal timescales provide estimates of extreme water level recurrence across the Salish Sea, capturing climate variability important to long-term coastal hazard planning. This approach has widespread applications for other complex estuarine systems.

Keywords: extreme water levels; sea level anomalies; storm surge; hydrodynamic modeling; climate change impacts; Salish Sea

check for updates

Citation: Grossman, E.E.; Tehranirad, B.; Nederhoff, C.M.; Crosby, S.C.; Stevens, A.W.; Van Arendonk, N.R.; Nowacki, D.J.; Erikson, L.H.; Barnard, P.L. Modeling Extreme Water Levels in the Salish Sea: The Importance of Including Remote Sea Level Anomalies for Application in Hydrodynamic Simulations. *Water* **2023**, *15*, 4167. https://doi.org/10.3390/w15234167

Academic Editor: Nick Cartwright

Received: 20 October 2023
Revised: 21 November 2023
Accepted: 23 November 2023
Published: 1 December 2023

Copyright: © 2023 by the authors. Licensee MDPI, Basel, Switzerland. This article is an open access article distributed under the terms and conditions of the Creative Commons Attribution (CC BY) license (https://creativecommons.org/licenses/by/4.0/).

1. Introduction

Coastal storms and associated flood impacts are projected to increase in extent and frequency as sea levels rise, adversely impacting communities, valued infrastructure, and critical ecosystems [1–4]. The mean rate of global sea level rise (SLR) has varied between 1.2 and 1.7 mm/yr in the twentieth century, has accelerated to 4.3 mm/yr over the last decade (2013–2022) [5], and is expected to further accelerate under most greenhouse gas emission scenarios [4,6–9]. Understanding and resolving extreme coastal water levels is therefore critical to assessing the future coastal impacts anticipated with changing atmospheric and ocean dynamics [10,11]. Numerical models can help quantify spatial variability in extreme water levels along coastlines that is not captured by the few sites monitored by water level gauges. Models and improved empirical data also help evaluate the relative importance of the environmental forcing terms leading to extreme water levels, which are important to forecasting future conditions related to climate change [12,13].

Extreme water levels commonly result from the co-occurrence of high tides and non-tidal residual (NTR) processes, including sea level anomalies (SLAs), inverse barometric pressure excursions, high winds, and other phenomena that contribute to water level anomalies above astronomically predicted values [14–16]. NTRs, defined here as all non-tidal effects on water levels, are commonly quantified by applying low-pass filters or subtracting predicted tides from measured water levels. They are applied to the boundary of hydrodynamic models as a time-varying summation in addition to astronomic tides. Sea level anomalies (SLAs) are one component of NTRs. They refer to deviations in the sea level from long-term (>monthly) mean levels, and they can be a significant driver of extreme water levels inside estuaries and coastal bays [14–19]. SLAs in the Eastern Pacific Ocean are driven by variations in ocean density (salinity and temperature), as well as winds, atmospheric pressure anomalies, regional current dynamics, and large-scale ocean phenomena such as El Niño Southern Oscillation (ENSO) and Pacific Decadal Oscillation [14,20–22]. Moreover, westerly and alongshore winds drive onshore wind setup and Ekman transport, resulting in a meridional jet and geostrophic setup along the U.S. west coast [23] that can propagate into inlets. Due to the wide range of processes that contribute to SLAs, they are difficult to predict using simple algorithms, and are most often approached using process-based numerical models.

Although SLA contributes significantly to extreme water levels and associated coastal hazards in Pacific Ocean coastal communities [24–30], long-term SLA data are sparse for wide-spread application in numerical simulations, and existing data have a wide range of uncertainty [31]. One dataset is the output from the HYbrid Coordinate Ocean Model [32] that provides sea surface height (SSH) data for 1994–2015, which can be analyzed for occurrences of SLAs. However, 22 years is a relatively short record for developing long-term statistics (e.g., 100 year water levels). While SLA data are vital offshore boundary conditions for hydrodynamic models [33], they are essentially nonexistent for use in future climate projections [34].

This paper describes a new approach to evaluate extreme water levels in estuaries and a methodology for representing remotely generated SLAs that can penetrate into these estuaries. First, we describe our study area in the Salish Sea and the development and validation of a hydrodynamic model for the Salish Sea (Figure 1). Next, we discuss the development of an empirically based SLA predictor by applying a multilinear regression of available wind, pressure, El Niño Index, and sea surface temperature anomaly (SSTA) data and discuss its validity by utilizing the derived SLA time series as the offshore boundary conditions for a hindcast scenario. To determine the relative importance of tides, SLAs, fluvial inflow, and other processes contributing to NTRs, the model was run with and without these forcing mechanisms. Lastly, extreme value analyses of a 30-year hindcast simulation were conducted to define and map the recurrence of the 2-year (50%) and 50-year (2%) water levels and NTRs in the Salish Sea and the relative contribution of SLA, pressure, and wind effects. The aim of this research is to advance a methodology to numerically simulate the contributions to extreme water levels efficiently in order to capture climate variability and change. The recurrence results and model accounting for decadal variability help inform resilience planning for coastal hazards. They also provide an approach to evaluate climate-scale changes to contributing factors that are relevant to complex estuary systems.

Study Area

The Salish Sea is a fjordal estuarine system located along the Eastern Pacific Ocean, spanning the border between the United States and Canada. It is home to two major population centers: Seattle, Washington (USA) and Vancouver, British Columbia, Canada (Figure 1). It includes three main basins connected through a complex network of channels and waterways, consisting of Puget Sound in the south, the Strait of Georgia in the north, and the Strait of Juan de Fuca in the west; the latter of which serves as the main connection with the Pacific Ocean. The existing population of 8.7 million bordering the Salish Sea is

projected to reach 10.5 million by 2040 [35]. Salish Sea coastal communities, infrastructure, and ecosystems are exposed to extreme water levels associated with the combined influence of tides, storms, and sea level rise [5,33,36–39]. Many of the lowest-lying coastal areas of the Salish Sea are vulnerable to flooding today and to anticipated sea level rise, which are national priorities for agriculture, recovering valued ecosystem services, salmon [40], and environmental justice where indigenous and other under-represented communities are disproportionately impacted [41,42].

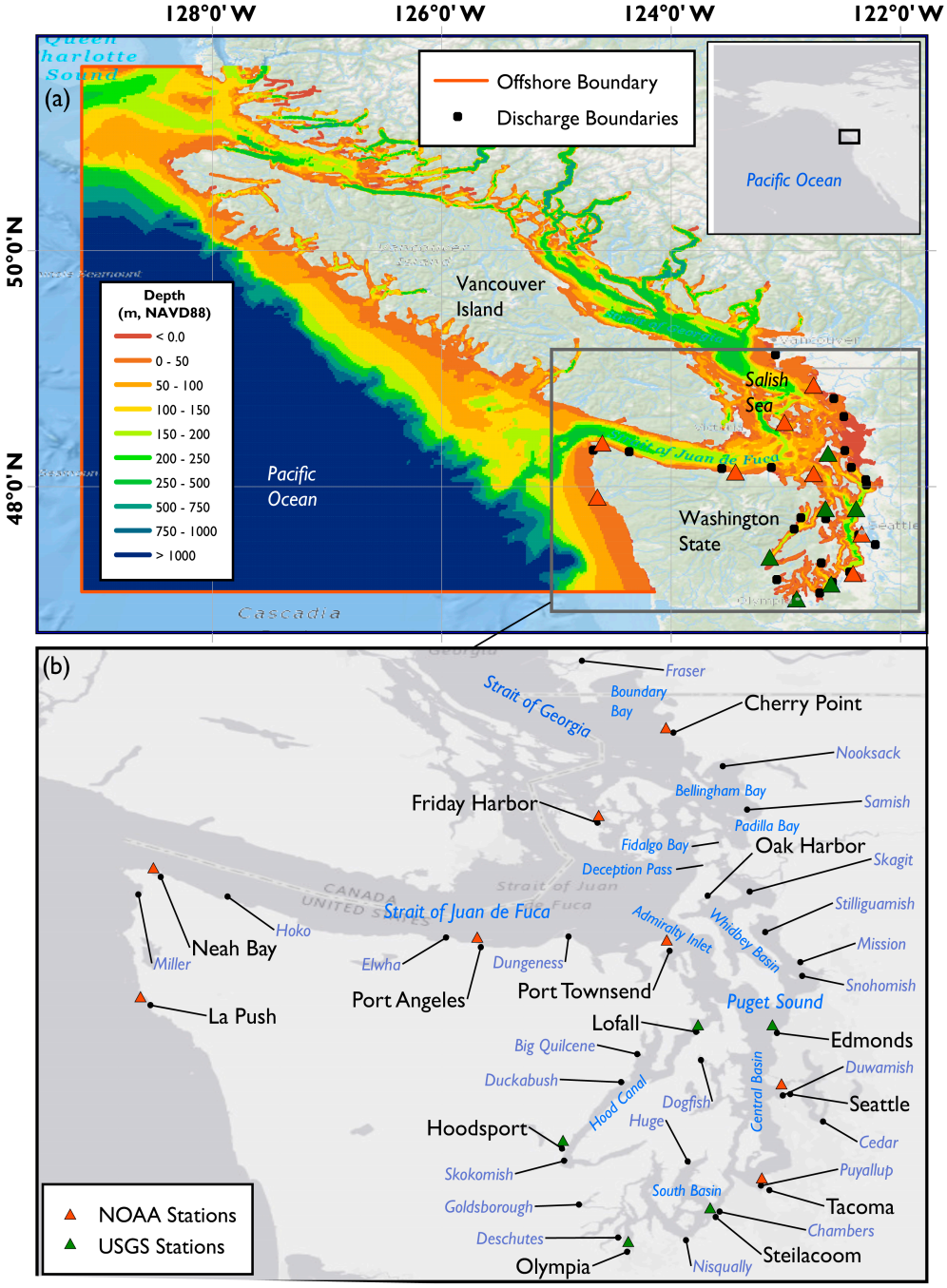


Figure 1. (**a**) Computational domain and bathymetry of the Salish Sea hydrodynamic model. (**b**) Locations of National Oceanic and Atmospheric Administration (NOAA, red triangles) and U.S. Geological Survey (USGS, green triangles) water level measurement stations.

Salish Sea tides are mixed-semidiurnal or mixed-diurnal, with a diurnal range of nearly 2.4 m at Neah Bay, increasing to 4.4 m at Olympia [43]. The tidal phase lag increases

with the distance from the ocean because of dissipation, and these increases are greatest at channels and inlets. Tidal currents can be strong—in excess of 1 m/s—in channels and inlets and weaker in basins.

Over the past decades, several studies have been conducted to better understand Salish Sea hydrodynamics, as well as the causes and spatial distribution of the extreme water levels in it [29,33,44–54]. These studies report that extreme water levels in the Salish Sea are primarily driven by low atmospheric pressure (inverse barometric effect) and winds, in addition to remote SLA that penetrate from the Pacific Ocean into the Salish Sea [28,47,53–55]. For example, in February 2006, SLAs were found to be the primary cause of a 70 cm NTR in the Salish Sea, and the contribution of local wind and atmospheric conditions was negligible [29].

2. Materials and Methods

2.1. Model and Data Sources

We developed a process-based hydrodynamic model following references [14,15] to capture the dominant physical forcing mechanisms contributing to extreme water levels in the Salish Sea. The Delft3D Flexible Mesh modeling suite (Delft3D-FM; 2020.04 release, SVN revision 66357, Delft, The Netherlands) was used to conduct the simulations. Delft3D-FM solves the shallow water equations [56] on a depth-averaged 2D horizontal (2DH) staggered unstructured grid. The model domain encompasses the entire Salish Sea (Figure 1a). The offshore boundaries extend north and west; therefore, the model domain includes the connection between the Strait of Georgia and the Pacific Ocean. In the south, the model boundary extends 180 km south of the entrance to the Strait of Juan de Fuca. The grid consists of 412,865 nodes, with resolutions varying between approximately 1 km at the seaward extents of the computational grid to approximately 150 m in Puget Sound and other coastal areas.

Three datasets were used to build the model bathymetry (Figure 1a). We used the U.S. Geological Survey (USGS) Coastal National Elevation Database topo-bathymetric digital elevation model (1 m resolution) for the Strait of Juan de Fuca [57] and Puget Sound [58]. Bathymetric data for the Strait of Georgia and other Canadian waterways in the northern Salish Sea were obtained from the National Oceanic and Atmospheric Administration (NOAA) 3 arc-sec (90 m) British Columbia digital elevation model (DEM) [59], and data gaps in the offshore were populated with the NOAA 30 arc-sec (900 m resolution) Strait of Juan de Fuca DEM [60]. Friction (roughness) values were initially obtained from available measured data [61]. All the bathymetry and water levels discussed in this work are relative to the NAVD88 vertical datum unless otherwise explicitly stated.

The roughness values were calibrated to optimize tidal propagation in the Salish Sea hydrodynamic model, with Manning's n coefficients ranging from 0.020 $s/m^{(1/3)}$ in the South Sound to 0.057 $s/m^{(1/3)}$ in the Strait of Juan de Fuca [62].

Oceanic boundaries were forced with tides and SLAs. FES2014 [63] global astronomical tide data with a resolution of 0.04 degrees was used to generate tidal boundaries. The phase and amplitude of tidal constituents and the vertical offset between the mean sea level and NAVD88 datum were calibrated iteratively based on differences between the modeled and observed tidal constituents at Neah Bay (see Figure 1 for locations). Time-varying, spatially uniform SLA for the calibration simulations were applied to the oceanic boundary either based on the HYCOM SSH data with a temporal resolution of three hours or based on the SLA predictor introduced in Section 3.2.

The hydrodynamics in the Salish Sea are strongly influenced by density variations, which can lead to mean sea level variations up to 0.5 m [44,45,64,65]. Accordingly, we generated a depth-averaged, normalized salinity field representing fall–winter conditions when extreme water levels are most prevalent. This was prescribed as an initial condition in the model at the beginning of each water year (WY, referred to as 1 October–30 September). Depth profile measurements of temperature, salinity, and density obtained by the State of Washington Department of Ecology Marine Waters Monitoring Program [66] were

converted into a spatial grid using triangular interpolation. Because the focus of this work was capturing extreme water levels in the Salish Sea, which mainly occur during the winter months, only the salinity data from October through March (1999–2017) were used for interpolation into the model. We used HYCOM global model salinity, temperature, and density data [31] for the period of 1993 to 2015 in the Strait of Juan de Fuca and the Pacific Ocean, where no measured data were available. Considering the measured and HYCOM density values, the equation of state was used to normalize the salinity values for a constant temperature of 12 °C [67]. We then used the normalized salinity field as the initial condition and excluded non-conservative temperature terms from the simulations, developing a robust and efficient Salish Sea hydrodynamic model.

Fluvial discharge was prescribed as the boundary conditions at the mouth of the 23 largest rivers entering the greater Puget Sound region [68,69] and the Fraser River [70] entering the Salish Sea (Figure 1). The mean daily discharge was used to capture the influence of stream flow on Salish Sea salinity and associated density-dependent coastal water level variability. Depending on the model period, different sources were used to prescribe these values (see Section 2.2). The model was additionally forced with spatiotemporally varying wind and pressure fields sourced from the Canadian 2.5 km High-Resolution Deterministic Prediction System (HRDPS) [71] and 6 km Weather Research and Forecasting (WRF) downscaling [72] of the North American Regional Reanalysis (NARR) [73].

2.2. Model Approach

The modeling was performed for two time periods (Table 1). The first simulation period, 1 October 2016 to 30 September 2020 (water years 2017 to 2020), was used to validate the Salish Sea hydrodynamic model. This period was chosen to make use of water level measurements at six USGS water level gages (Figure 2a) in areas of limited existing observations (e.g., Whidbey Basin and Hood Canal), complementing data from eight existing NOAA tide gauges (Figure 2b). The water levels used in reference [74] were collected at 15 min intervals spanning the period from November 2018 to June 2020 and referenced to the vertical datum NAVD88 with a maximum uncertainty of 3 cm. For this validation period, we used hourly wind and atmospheric pressure data sourced from the 2.5 km HRDPS numerical weather model and HYCOM SSH data to represent SLAs for boundary forcing. The model simulations were performed as individual water years and merged into a single four-year time series (2017, 2018, 2019, 2020).

Table 1. Model period, purpose, time period, and sources of sea level anomaly (SLA): streamflow and meteorological conditions.

	Model Period	Purpose	Time Frame	SLA	Streamflow	Meteorology
1	Short-term detailed historical period	Determine model skill using the best available data	2017–2020	HYCOM	USGS, Environment and Natural Resources Canada ‡	HRDPS
2	Long-term historical period	Validate SLA predictor Estimate extremes and contributions	1985–2015	HYCOM *; SLA predictor †	USGS, Environment and Natural Resources Canada ‡	WRF-NARR ‼

Notes: * 1994–2015; † 1985–1994; ‡ gap-filled multi-linear regression (see Appendix A.1); ‼ meteorological bias correction (see Appendix A.2).

The second period, spanning 1985–2015, was used to test the skill of the derived sea-level anomaly predictor and quantify extreme values in the Salish Sea. For these analyses, HYCOM SSH was prescribed along the offshore boundary for the period of 1995–2015. Following a comparison of the SLA predictor calculated using the multi-parameter regression and WRF downscaled NARR outputs (see Sections 2.3 and 2.4 for details) to HYCOM over the period of 1995–2015 that showed comparable skill, the SLA predictor was used for the period of 1985–1994, prior to the availability of HYCOM.

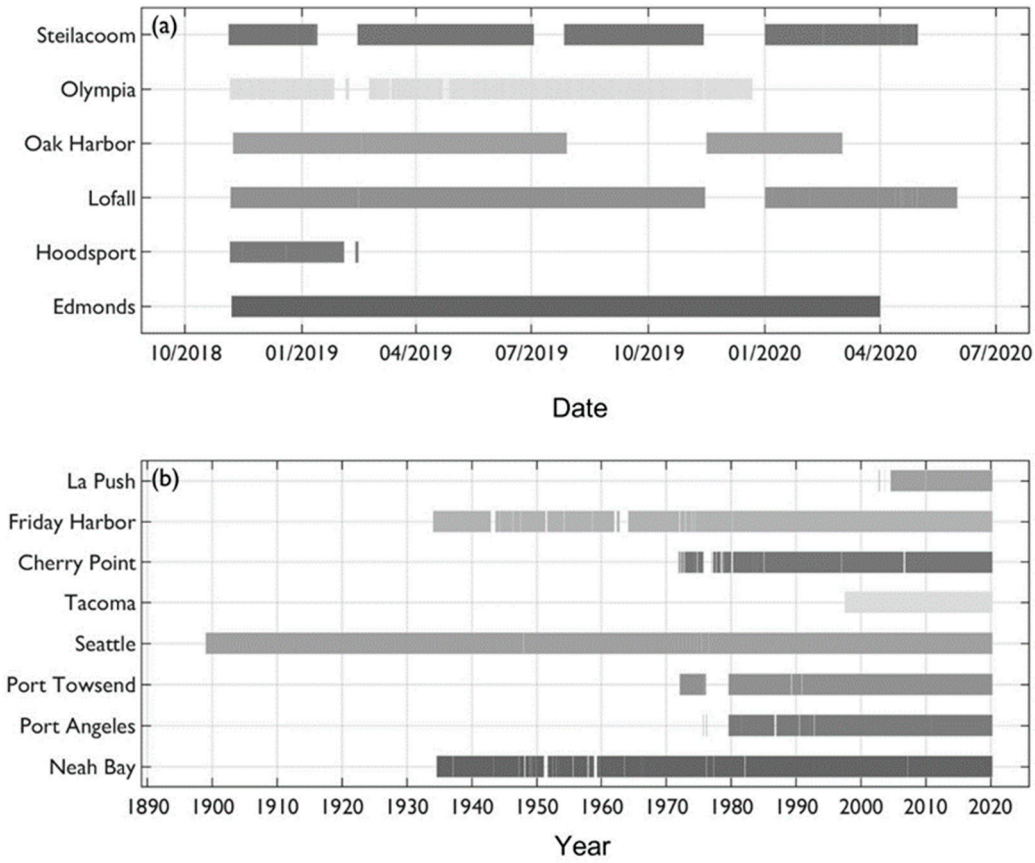


Figure 2. Timeline of available water level data at the U.S. Geological Survey (**a**) National Oceanic and Atmospheric Administration (**b**) water level stations. Locations of measurement sites shown in Figure 1B.

2.3. Analysis Methods

The tidal constituents, including amplitudes and phases, were calculated from the continuously measured water levels at each station using UTide [75]. The predicted tidal water levels that were calculated from the constituents were subtracted from the measured water levels to provide estimates of NTRs at each observation location.

Stream discharge data containing temporal gaps were filled using a multi-linear regression against other available sites. The regression included a temporal offset parameter for each site in the regression, determined based on the greatest correlation discharges. A similar procedure was used to predict future discharge at streams not modeled in the downscaled hydrological simulations available as part of the University of Washington Climate Impacts Group Pacific Northwest Hydroclimate Scenarios Project [76]. Additional details of the gap-filling approach are provided in Appendix A.1.

Wind speed predictions from 6 km WRF downscaled NARR simulations [72] were adjusted to better represent the wind over the water, as coarse numerical weather products commonly underpredict the wind over water in narrow bays and inlets, where higher friction has been parameterized for land. The comparatively high-resolution 2.5 km HRDPS and observations at NOAA coastal meteorology stations were used to develop a bias correction for extreme wind (99th percentile). The correction was applied to historical and future predictions following the details described in Appendix A.2.

To assess the accuracy of the model, several skill score metrics were used, including the model bias, mean absolute error (MAE), root mean square error (RMSE), coefficient of determination (R^2), and scatter index (SCI), which is RMSE divided by the mean of observations at each measurement point. The SCI gives a relative measure of the RMSE compared to the observed variability.

An annual maxima/generalized extreme value (AM/GEV) analysis [77] was used to compute the extreme recurrence of water levels. We used the open-source "pyextremes" library to perform the GEV analysis on model-derived spatial annual maximum water levels at each grid cell from the 1985–2015 hindcast. To assess the reliability of the AM/GEV analysis, we also applied a peak-over-threshold/generalized Pareto distribution (POT/GPD) approach and found comparable results to the values calculated using the AM/GEV method. Whereas the POT method is often considered more robust for evaluating extreme values compared to the AM/GEV method [77], we used the AM/GEV approach for its computational efficiency to generate extreme water level recurrence for each model cell across the model domain from Delft3D outputs of the annual maxima.

2.4. Development of Sea Level Anomaly Predictor

We developed an SLA predictor to provide forecast capabilities for SLAs that are important to understanding current sources of extreme water levels and potential changes to extreme water levels in the future. First, we tested the correlation between the modeled and measured NTR at the entrance of the Strait of Juan De Fuca at Neah Bay based on different spatially explicit prescriptions of the SLA along the offshore marine boundary. In particular, the SLA is based on HYCOM SSH data at different locations along the open ocean boundary of the Salish Sea hydrodynamic model. These tests were used to identify a single location with the highest correlation between the modeled and measured NTR at Neah Bay. The correlation tests demonstrated that the NTR and extreme water levels at Neah Bay are most sensitive and are most highly correlated with SLA forcing 5 to 10 km offshore along the southern boundary of the Salish Sea model. Therefore, this arbitrary location was used in this study instead of nesting the hydrodynamic model with spatially varying HYCOM values along all open ocean boundaries.

Second, we formulated a multi-parameter SLA predictor for the estimation of remote NTRs for periods when modeled SLA data do not exist. The SLA predictor was initially determined by testing the individual correlation between four physical processes to HYCOM SSH data during the 1995–2010 water years. Wind stress estimates from dynamic and geostrophic winds (τ), ENSO indices, and offshore sea surface temperature and pressure anomalies were found to have the most significant correlations to the HYCOM SSH data. Physical processes such as Ekman pumping and Pacific Decadal Oscillation showed negligible correlations with the HYCOM SSH data. For this analysis, we used the WRF downscaled NARR wind and pressure fields spanning the period 1985–2015 [70]. Wind stress was discretized to daily values consistent with the Oceanic Nino Index, SST, and SSP variables used to capture their influence on sea surface height variations operating at daily timescales or longer [78,79]. After investigating the correlation of each physical parameter individually to HYCOM SSH data at the selected offshore model boundary sites, multivariate regression was used to identify the optimal time lag for each term. The time lags were determined based on individual lagged correlations, using the lag associated with the highest correlation. As the final step for developing the SLA predictor, the regression results were quantile-corrected to have the same distribution as the HYCOM SSH data. The final SLA predictor took the form of the following formulation:

$$\text{SLA predictor} = 0.47\tau y - 0.000053\ (\text{SLPA}) + 0.024\ (\text{SSTA}) + 0.021\ (\text{ONI}) \quad (1)$$

where τy (N/m^2) is dynamic northward wind stress, SLPA (Pa) and SSTA (°C) are sea-level pressure and sea-surface temperature anomalies, respectively, and ONI is the Oceanic Nino Index (°C).

3. Results

3.1. Model Skill: Tides and Storm Surge Propagation, Water Level Gradient

The model skill was assessed by comparing the values between the modeled and measured water levels for each observation station over the four-year validation period (2017–2020 water years), showing good agreement (Figure 3). Positive and negative bias

values indicate over- and underestimates of the mean water levels, respectively. The total RMSE varied between 9.4 cm and 18.5 cm for the Edmonds and Hoodsport stations, respectively. The lower skill at Hoodsport may be due in part to the shorter observation period (~4 months) and poorer representation of the initial density field and fluvial inputs.

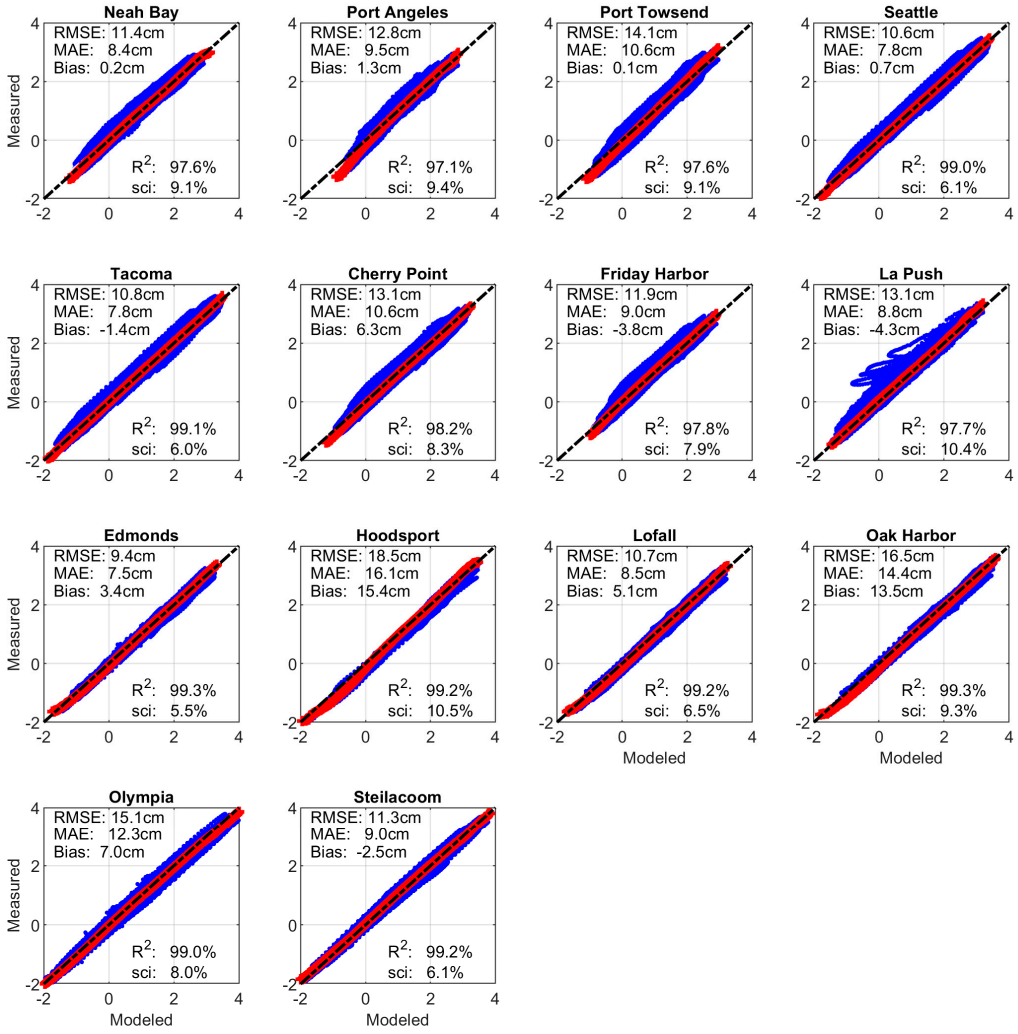


Figure 3. Modeled and measured water levels: quantile–quantile (Red) and scatter (Blue) plots for the Salish Sea hydrodynamic model validation period (2017–2020 water years) in meters relative to NAVD88. The root mean squared error (RMSE), mean absolute error (MAE), mean averaged error (bias), correlation of determination (R^2), and scatter index (sci) values for each measurement station are listed.

The amplitude and phasing of the largest astronomic tidal constituent (M2) across the sites are represented well (Figure 4A,B). Along the trajectory from the Strait of Juan de Fuca into South Puget Sound, the amplitude of M2 initially decreases sightly then steadily increases. The maximum amplitude and phase of the M2 tide of ~1.2 m and ~5.5 h, respectively, agree with the observed values (Figure 4D,E), along with other dominant constituents (K1, O1, S2, N2). Furthermore, the model is able to represent the overall increase in the mean water level observed between Neah Bay and South Puget Sound that is related to the estuarine circulation and density effects of the complex fjordal estuarine system (Figure 4C,F). The modeled mean water level along the regional transect evaluated (white line in Figure 4C, black line in Figure 4F) over the period of 1 October 2017 to 30 September 2020 agrees with the observed values at the NOAA tide gages (circles in Figure 4C,F; crosses denote modeled mean water levels at gage sites).

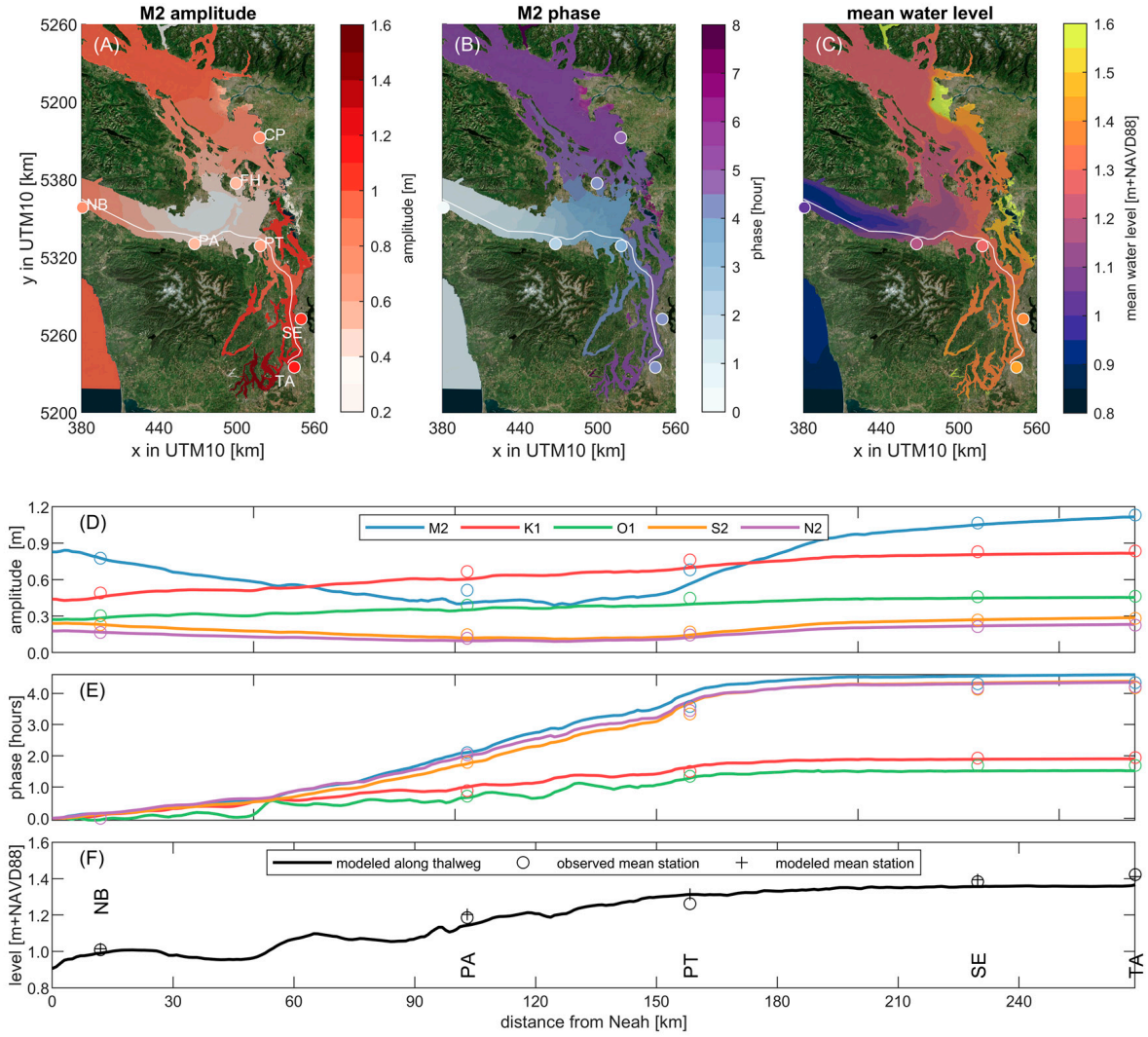


Figure 4. Maps of modeled M2 tidal amplitude in meters (**A**), M2 tidal phase in hours (**B**), and mean water level in meters (NAVD88) (**C**) during the 2017–2020 water years. Measured values are shown with circles. Plot of amplitude (**D**), tidal phase (**E**) of M2, K1, O1, S2, and N2 tidal constituents, and mean water level (black line in (**F**)) along the profile (white line shown in (**C**)) relative to the observed mean levels at tide gages Neah Bay (NB), Port Angeles (PA), Port Townsend (PT), Seattle (SE), and Tacoma (TA); crosses denote modeled mean water levels at gage sites as opposed to along the offshore transect; errors are similar to or smaller than the circles.

Target plots (Figure 5) show the bias and bias-removed RMSE for the water levels at each measurement station. The comparisons include error metrics for the modeled tides, NTRs, water levels, and water levels exceeding the 50th, 90th, 95th, and 99th measured percentiles to highlight the model's performance in capturing extremes. The modeled tidal amplitude and phase errors are generally minor, with an average uRMSE of less than 10 cm (brown triangles in Figure 5). The simulated water levels over the entire 2017–2020 validation period had RMSEs less than 15 cm at all measurement stations except at Hoodsport (18.5 cm), Olympia (15.1 cm), and Oak Harbor (16.5 cm) (Figures 3–5). However, the model captures high water levels more accurately with lower RMSE values for modeled water levels above 99th percentile at Hoodsport (11.8 cm), Olympia (13.9 cm), and Oak Harbor (11.1 cm). The error values for the modeled water levels are driven by differences in the tide and NTR (notice triangles and diamonds in Figure 5). Note that the NTR estimations are defined as the residual water levels after removing the tide, and they include the effects, for example, of the SLA, mean sea level, and wind-driven setup.

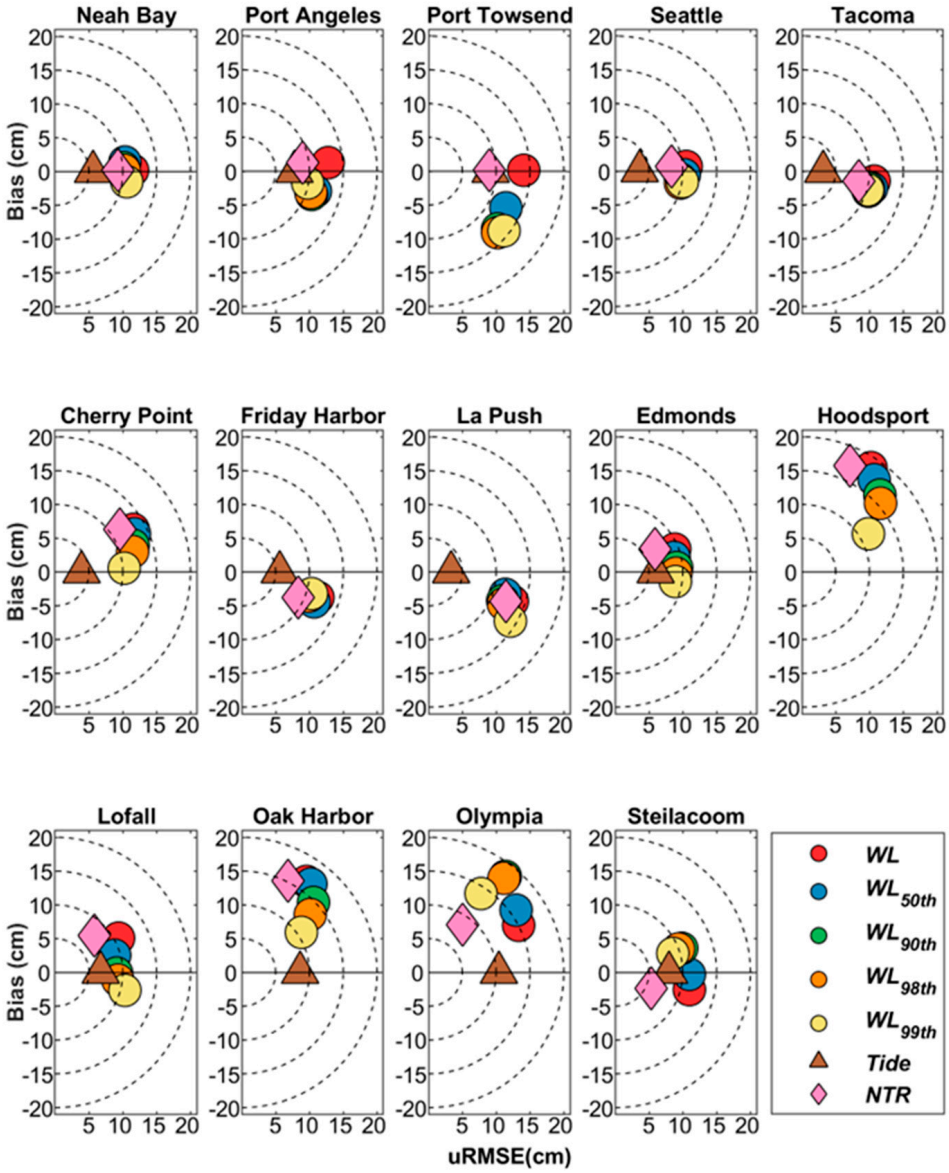


Figure 5. Unbiased root mean squared error (uRMSE) and bias values for the modeled water levels (WL) (red circles) and water levels above the 50th (blue circles), 90th (green circles), 95th (orange circles), and 99th (yellow circles) measured percentiles during the 2017–2020 water years. Brown triangles and pink diamonds show error values for the tide and non-tidal residual (NTR). The polar distance from the center shows the RMSE values at each station ($uRMSE^2 + Bias^2 = RMSE$).

3.2. Sea Level Anomaly Predictor

The quantile-corrected SLA predictor at the model boundary had an RMSE of 5.5 cm ($R^2 = 0.76$) relative to HYCOM SSH over the period of 1995–2010, with slight underestimations of the highest SSH anomalies (Figure 6A). The variability in the RMSE of the modeled SLA over the simulated period ranged from 4.2 to 6.2 relative to HYCOM SSH (Figure 6B). The predictor showed better agreement with HYCOM SSH during more extreme winter high water level anomalies (Figure 6C).

The simulated water level, tide, NTR, and water levels exceeding the 99th percentile based on the SLA predictor and HYCOM forcing on the offshore boundary over the 15-year hindcast period of 1995–2010 agree within 5–15 cm across all stations (Figure 7). The differences in the RMSE for the water levels forced by the predictor versus HYCOM were 1 cm at all the measurement stations except for Cherry Point, where the RMSE with the SLA predictor model was ~2 cm higher than the model prescribed with HYCOM SLA.

However, the simulations that used the SLA predictor as the offshore boundary condition had better skills for predicting water levels above the 99th percentile, highlighting that the developed predictor is a reliable tool for estimating extreme water levels. Overall, the results of this validation effort confirmed the SLA predictor as an appropriate offshore boundary forcing alternative for the Salish Sea hydrodynamic model when other SLA datasets are unavailable.

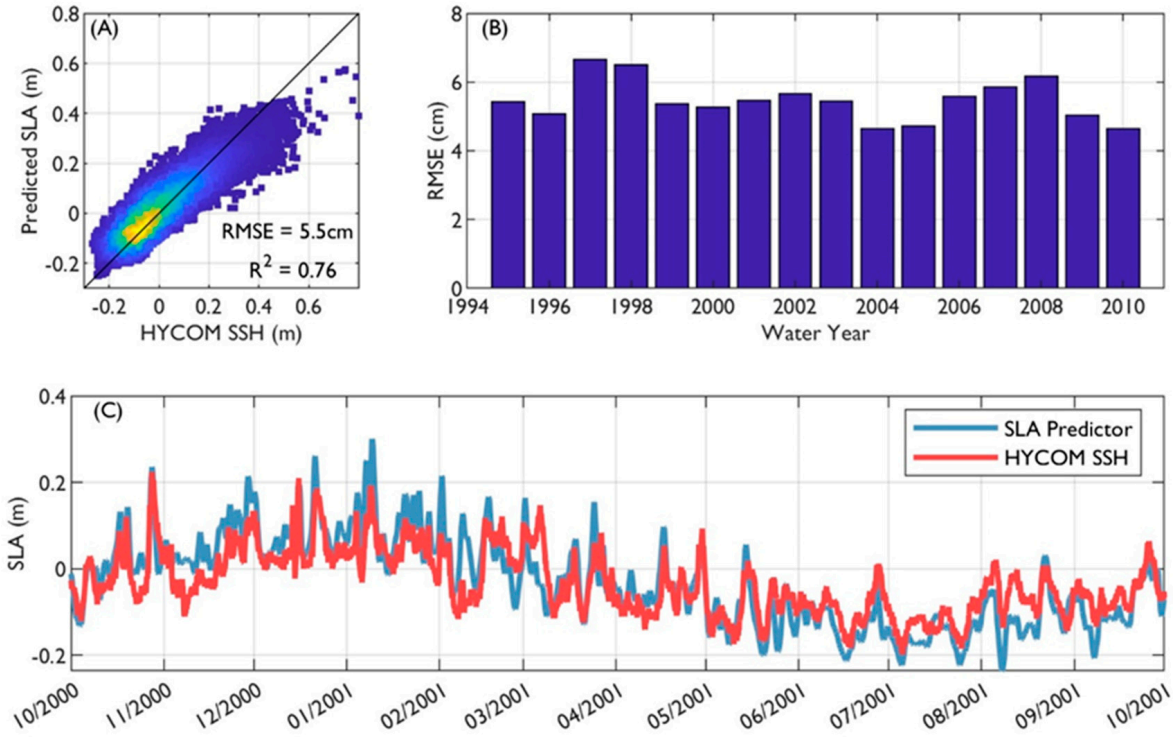


Figure 6. (**A**) Scatter plot of the SLA predictor compared to the HYCOM SSH data at the offshore model boundary (warmer colors represent higher frequency of occurrence). (**B**) SLA predictor RMSE with respect to HYCOM SSH data for water years 1995–2010. (**C**) Time series of SLA predictor (blue) and HYCOM SSH (red) for the 2001 water year.

3.3. Extreme Water Level Recurrence and Change

The model skill for predicting water levels over the long-term historical period (1985–2015) in terms of the RMSE was better than 16 cm at all the stations, with an average RMSE of 12 cm (Figure 8). No significant trends in the RMSE across stations and years were observed. However, the model skill at La Push was slightly poorer in the first years of comparison (WY2003–2004). The water levels in WY1997 had an above-average RMSE, which became especially clear for the stations in Cherry Point and Seattle. Cherry Point, in particular, had the most variability in RMSE of all the stations included in this comparison.

The extreme recurrence based on the AM/GEV and POT/GPD distributions of the modeled and measured water levels at the NOAA Seattle tide gage station are similar (Figure 9 red and blue lines). The AM/GEM extreme water level estimates based on the modeled water levels (green line) are typically similar (within 5 cm) to the values derived from the measured water levels. This similarity between results was consistent for the other stations, confirming the validity of the AM/GEV method for estimating extreme water levels and using the 1985–2015 hindcast water level values. However, for frequent events (e.g., annual events), differences were noticeable between the approaches.

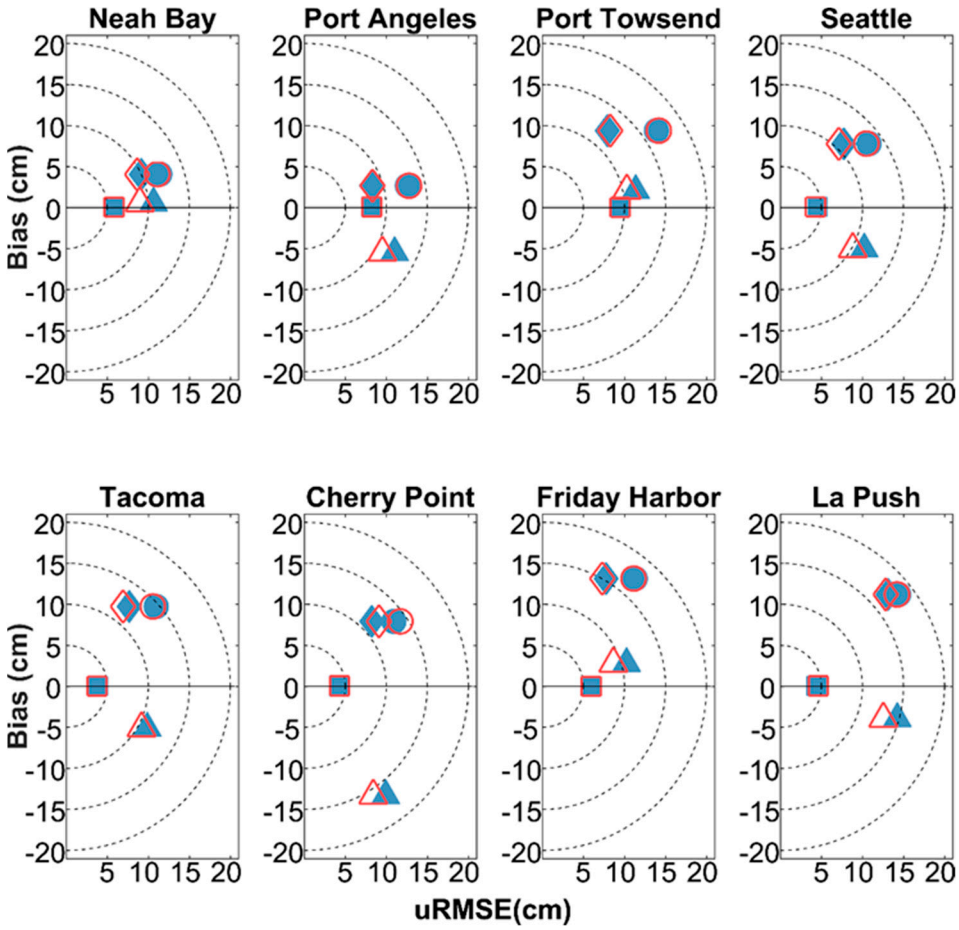


Figure 7. Unbiased root mean squared error (uRMSE) and bias for the modeled total water level (circles), tide (squares), non-tidal residuals (NTR, diamonds), and water levels above 99th percentile (triangles) using HYCOM SSH (solid blue) and SLA predictor (hollow red) as offshore boundary conditions. The polar distance from the center shows the RMSE values at each station ($uRMSE^2 + Bias^2 = RMSE$).

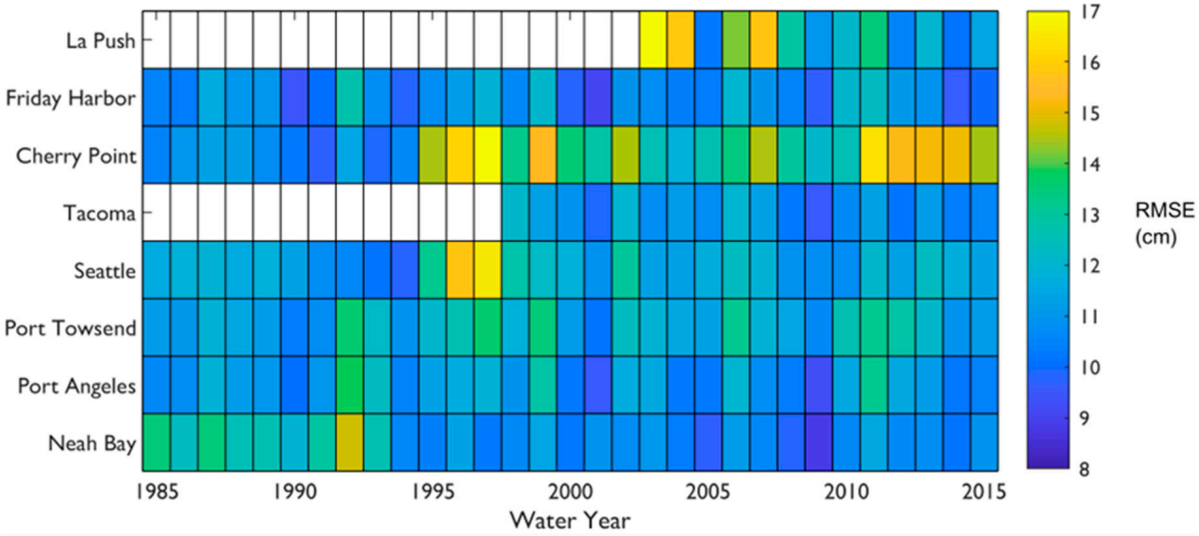


Figure 8. RMSE of modeled water levels above MSL for water years 1985–2015 at the NOAA measurement stations (Figure 1). The color bar values are in cm, and empty squares indicate unavailable measured data.

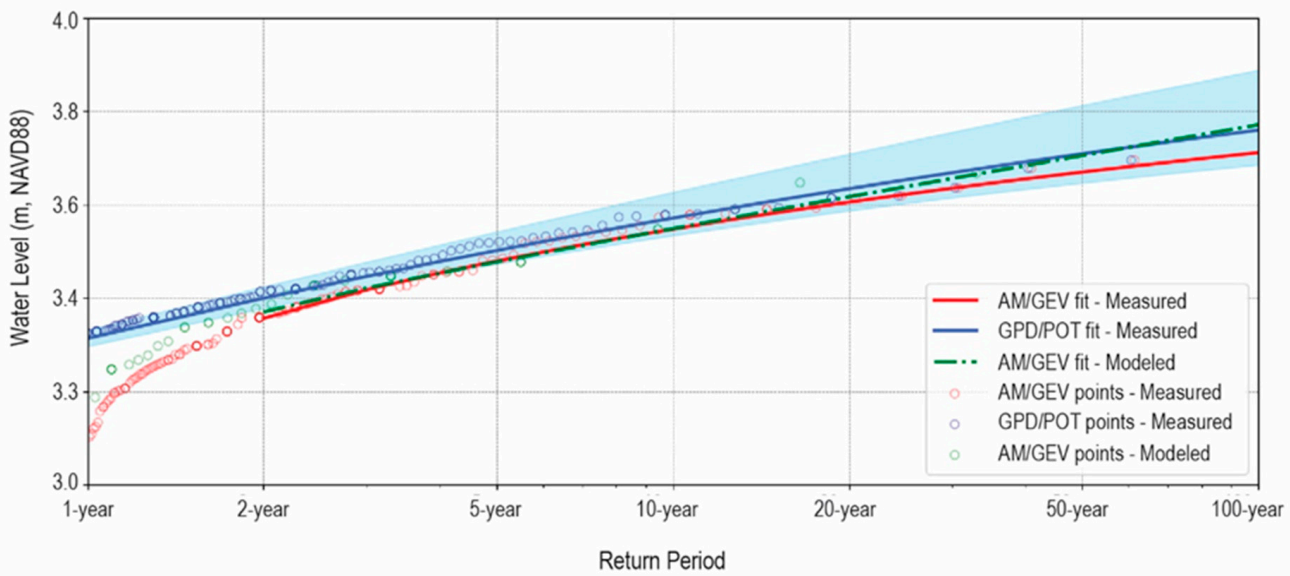


Figure 9. Extreme value analysis for Seattle (NOAA station ID, 9447130) based on the POT (blue) and AM/GEV method (red) for the modeled and measured water levels. Circles are point estimates used to fit the representative distribution, and the blue shading shows the 95 percent confidence interval for the POT method. The AM/GEV results of modeled water levels are shown with the green dotted line.

Because the hindcast duration was limited to 31 years and AM/GEV theoretically cannot assess 1-year water levels, we characterized low- and high-probability extreme water levels based on modeled 2-year and 50-year water levels (Figure 10). The modeled 2-year (50%) and 50-year (2%) extreme water levels across the Salish Sea demonstrate higher extreme water levels in Puget Sound than the Strait of Juan de Fuca and the Strait of Georgia. Among the different basins of Puget Sound, the modeled extreme water levels were highest in South Sound, with 50-year water levels mostly above 4.0 m NAVD88. Whidbey Basin showed the next-highest values, with 50-year water levels ranging between 3.5 and 3.9 m NAVD88, while in Central Basin and Hood Canal, the 50-year water levels ranged from 3.3 to 3.7 m NAVD88.

In contrast to the extreme water level distribution pattern shown in Figure 10 that largely reflects tidal behavior (Figure 4A,B), the AM/GEV analysis performed for the 1985–2015 reanalysis simulations without tidal forcing and assuming no interactions between tides and NTR [16] showed different extreme NTR distributions (Figure 11). The modeled 2-year (50%) and 50-year (2%) NTR are smaller inside Puget Sound than in other bodies of water in the Salish Sea. This highlights the increasing importance of tide to extreme water levels deeper into the Salish Sea. The NTRs are modeled 0.1–0.3 m higher across the shallow embayments and river deltas of Boundary, Bellingham, Padilla, and Fidalgo Bays and Whidbey Basin. The 2-year and 50-year NTR recurrence derived using the model and SLA predictor show good agreement with those calculated based on the measured values (Figure 11, circles at stations).

3.4. Contribution of SLA to Extreme Water Levels

Extreme value analyses differencing the individual SLA-, atmospheric pressure-, and wind-specific hindcast (1985–2015) simulations from the 'combined' water level results by excluding one of these forcing mechanisms for each analysis indicate that SLA plays the greatest relative role to extreme water levels across the Salish Sea (Figure 12). Excluding SLAs from the simulations resulted in 30 to 60 cm underestimations of NTR in parts of Puget Sound and the Strait of Georgia (Figure 12A,B). Atmospheric pressure was next in importance, as the 2- and 50-year water levels were underestimated by an average of 15 cm and 25 cm, respectively, when the pressure effects were neglected. Additionally, the model

results demonstrated that wind contribution to extreme water levels is generally small in the Salish Sea, except in the northern areas of the Strait of Juan de Fuca and Southern Strait of Georgia, where the 50-year water levels would be underestimated by 15 to 20 cm if the wind effects were neglected. Understanding the relative roles of forcing factors is anticipated to be increasingly important to address changes in future climate and sea level and the effects of their interactions on extreme water levels.

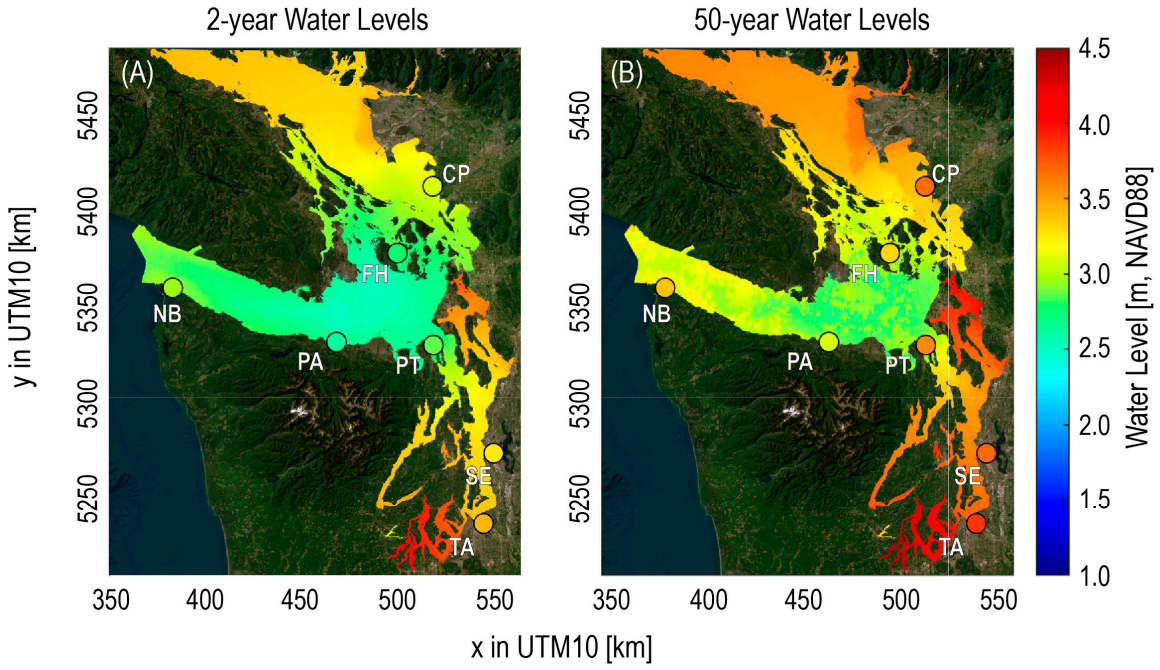


Figure 10. Modeled 2-year (50%) and 50-year (2%) water levels across the Salish Sea in NAVD88. Circles depict estimates based on measured values.

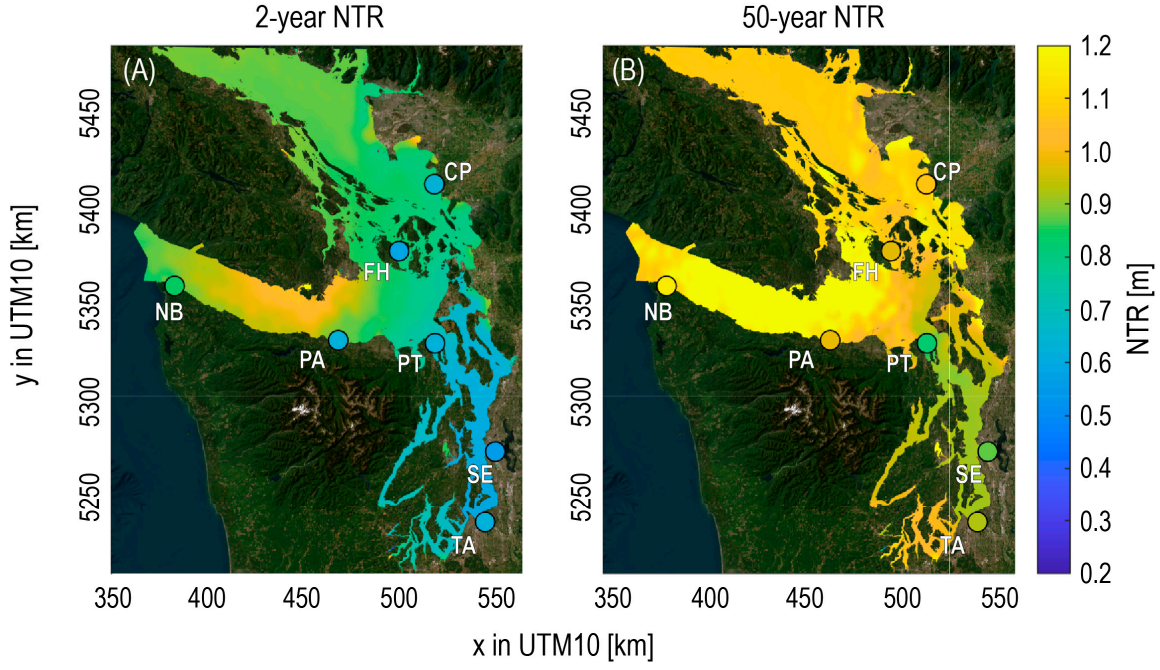


Figure 11. 2-year (50%) and 50-year (2%) non-tidal residuals (NTR) in the Salish Sea based on the extreme value analysis (EVA) using the hindcast results for the 1985–2015 water years. Circles depict estimates based on measured values.

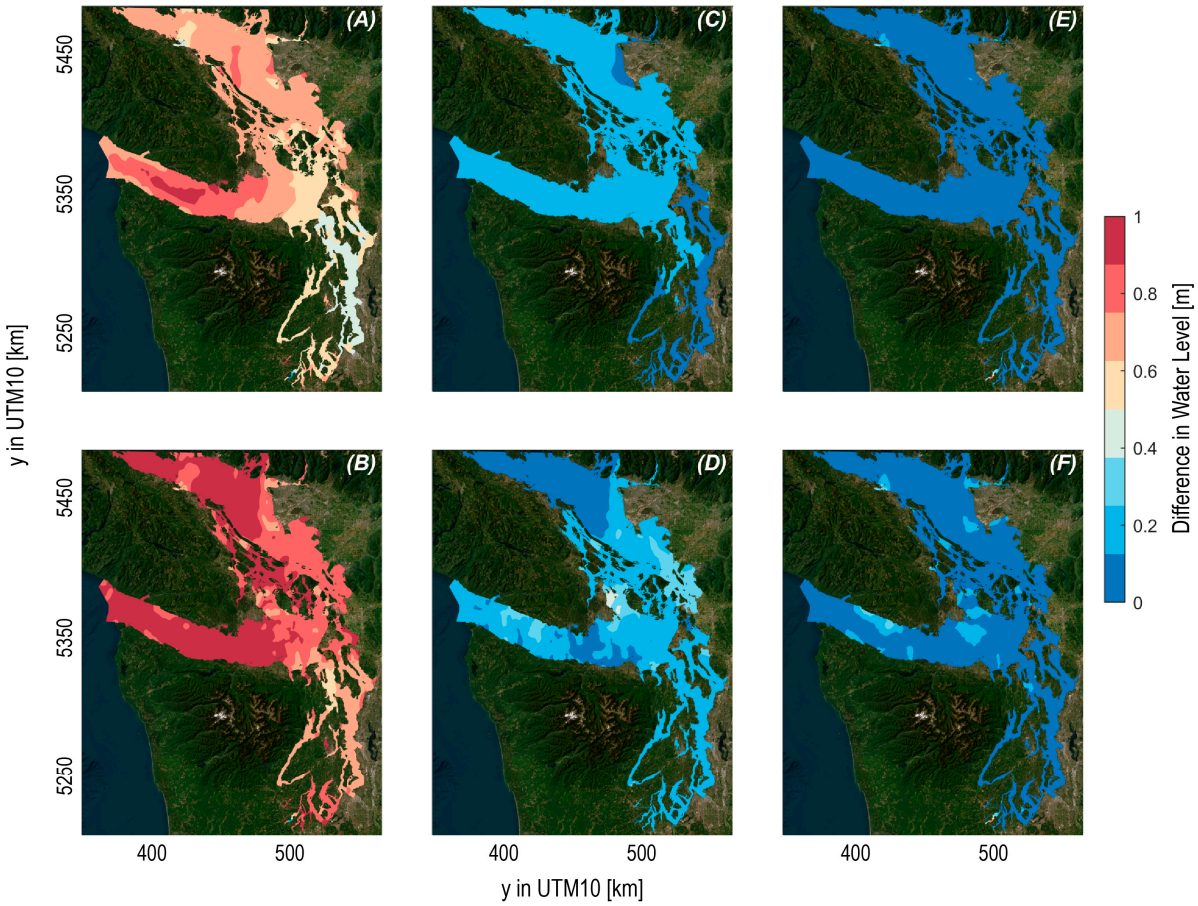


Figure 12. Underestimation of 2-year (**A**,**C**,**E**) and 50-year (**B**,**D**,**F**) NTRs if sea level anomalies (**A**,**B**), atmospheric pressure (**C**,**D**), and wind (**E**,**F**) effects are neglected. Values are in cm.

4. Discussion

The validation presented here shows that the depth-averaged Delft3D FM model can accurately simulate extreme still water levels (defined here as absent wave height and wave runup) throughout the Salish Sea for the detailed validation period from 2017 to 2020 (Figures 3 and 5) and for the longer-term hindcast of 1985 to 2015 (Figure 8). This accuracy has been achieved by identifying the density variations that influence the mean sea level and the creation of an SLA predictor. The advantage of this approach is that it is possible to simulate the hydrodynamic conditions in the Salish Sea over decades to ensure reliable input data for the extreme value analysis. Furthermore, capturing sufficient environmental variability enabled the determination of the relative role of important drivers of extreme water levels, including remotely generated sea level anomalies relative to local and regional atmospheric pressure and wind effects. The downside of this approach is that depth-averaged modeling for salinity and temperature prevents us from representing three-dimensional estuarine hydrodynamics. Using an initial salinity field accounting for fall and winter conditions addresses the difficulties reported in other efforts [29,80,81] in capturing M2 tidal harmonics in the Salish Sea when extreme water levels are prominent. However, due to depth-averaged model limitations, the model does not capture the evolution of density with the transition from winter to summer conditions, and it overestimates the mean sea level during the second half of a water year (~spring and summer conditions). We also do not account for annual variations in salinity. We suspect that the difficulty of capturing the mean sea level using a depth-averaged model might explain the relatively large biases at, for example, Hoodsport and Oak Harbor. Moreover, the relatively large calibration range for friction values indicates model inaccuracies (e.g., bathymetry or grid discretization) or processes not included in the model (e.g., 3D effects). Lastly, this work

does not consider the effects of waves. Instead, it focuses on computing extreme still water levels caused by tide, mean sea level, remotely generated SLA, and local atmospheric pressure and winds relevant to evaluating the effects of climate change and sea level rise.

A critical component of our modeling approach is the SLA predictor. For the period from 1994 to the present, HYCOM-based SSH was used for the SLA, resulting in the highest model skill. However, the lack of SSH data like HYCOM prior to 1994 and for future time periods has limited the long-term simulations required to determine robust extreme water level recurrence. The SLA predictor introduced in this paper is a pragmatic approach that employs readily available hindcast and projected parameters. The SLA predictor facilitates assessments beyond the limited time period of measured SLA and evaluates potential changes in the future, assuming relationships between the observed SSH and forcing parameters. The extent to which relationships between SSH and forcings diverge in the future from those observed in the past may be important and will be a focus of additional research given the importance of SLA to coastal flooding.

Four different model simulations with and without the following individual boundary condition forcings were used to determine the recurrence water levels and the relative contributions of tides, SLA, atmospheric pressure, and wind to extreme still water levels. This pragmatic approach applied across San Francisco Bay [16] also worked well to estimate the return probability of still water levels across the Salish Sea and to quantify the individual effects of dominant forcing mechanisms. The NTR values and distribution patterns were similar to estimates from other studies based on shorter simulations [54]. The extreme water levels and NTRs modeled here, based on a 30-year period, allow for more robust extreme value analyses capturing decadal-scale climate variability, which is important for diverse planning applications. Our findings indicate relatively higher and therefore greater exposure to extreme water levels in South Puget Sound, Whidbey Basin, and the regions of Boundary Bay, Bellingham, Samish, Padilla, and Fidalgo Bays (Figure 10). Localized higher exposure to extreme NTRs are also modeled in these areas (Figure 11), in part related to local atmospheric pressure and wind effects interacting with the broad and shallow river delta and embayment environments (Figure 12).

Resolving the relative contributions to extreme water level recurrence provides a unique approach to assess the influence of discrete processes that lead to flooding, including remotely generated SLAs that penetrate into the Salish Sea from the Pacific Ocean and can contribute 50–60% of the total water level anomaly inside the estuary. Accounting for individual drivers of extreme water levels, including the remotely generated SLA, is important for coastal flood prediction, as each of these drivers are anticipated to respond to climate change and sea level rise in unique and complex ways. Informing the expected increase in coastal flooding with change in climate and sea level rise [2,3] will benefit from further research and refinement of environmental factors like SLA and uncertainty that drive extreme water levels and NTRs.

5. Conclusions

Here, we have presented a new method for estimating sea level anomalies (SLAs) and modeling extreme water levels in the Salish Sea. The hydrodynamic model successfully captured the dominant physical forcing mechanisms contributing to extreme water levels across the complex geomorphology and hydrodynamics of the estuary. The model showed good agreement with measured water levels, tides, and non-tidal residuals (NTRs), indicating its skill in simulating the hydrodynamics. The validation results demonstrated that the model accurately represented the amplitude and phase of the dominant astronomic tidal constituents (M2, K1, O1, S2, N2) and the overall increase in the mean water level into the estuary. Additionally, the accuracy of the modeled water levels improved for more extreme water levels.

To estimate SLAs for periods when SLA or SSH data are unavailable, we developed a multivariate regression-based SLA predictor. The predictor considered the effects of the sea level pressure anomaly, sea surface temperature anomaly, wind stress, and El

Niño Southern Oscillation Index. The validation of the SLA predictor using HYCOM SSH data showed good agreement, with an RMSE of 5.5 cm and a high correlation (R^2 = 0.76). The SLA predictor was successfully applied as the offshore boundary condition for the hydrodynamic model, facilitating reliable estimates of extreme water levels.

Extreme water levels and their recurrence, capturing decadal climate variability, were generated across the Salish Sea by applying the developed model and SLA predictor to a 30-year hindcast re-analysis for the period of 1985–2015. The high model accuracy facilitated the evaluation of the relative contribution of sources to extreme water levels. The model results revealed that remotely generated SLAs play a dominant role, explaining 50–60% of the variability in extreme water levels inside the Salish Sea. Additional contributions include atmospheric pressure anomalies and local winds inside the Salish Sea. A greater tide range and mean sea level reached into the deeper areas of Puget Sound and combined with a complex distribution of extreme NTRs to make extensive areas of South Puget Sound, Boundary Bay near the Canadian border, and the large river delta/bay environments of Bellingham, Samish, Padilla, Fidalgo Bays, and Whidbey Basin more exposed to extreme water levels than the other coastal areas evaluated.

Overall, this study advances a framework and contributes to a better quantitative understanding to model the sources of extreme water levels, including the role of remotely generated SLAs in estuaries. The models provide a reliable and flexible approach for assessing past and future coastal impacts. The developed hydrodynamic model and the SLA predictor can serve as valuable tools for coastal management and decision-making, helping to mitigate the potential risks posed by sea level rise and changing atmospheric and ocean dynamics, some of which may manifest from remote sources.

Author Contributions: Conceptualization, E.E.G., A.W.S., L.H.E. and P.L.B.; methodology, E.E.G., B.T., C.M.N., A.W.S. and L.H.E.; software, B.T., C.M.N. and A.W.S.; validation, B.T. and D.J.N.; formal analysis, E.E.G., B.T., C.M.N., A.W.S., S.C.C. and N.R.V.A.; investigation, E.E.G., B.T., C.M.N., S.C.C., A.W.S. and N.R.V.A.; resources, E.E.G. and P.L.B.; data curation, E.E.G., B.T. and D.J.N.; writing—original draft preparation, B.T., C.M.N., E.E.G. and S.C.C.; writing—review and editing, E.E.G., C.M.N. and A.W.S.; visualization, E.E.G., B.T., C.M.N. and S.C.C.; supervision, E.E.G.; project administration, E.E.G.; funding acquisition, E.E.G. and P.L.B. All authors have read and agreed to the published version of the manuscript.

Funding: Funding and support for this study were provided by the U.S. Environmental Protection Agency (DW-014-92478501-0) and U.S. Geological Survey (USGS) Coastal and Marine Hazards and Resources Program.

Data Availability Statement: Data and model set-up files are provided in [62].

Acknowledgments: The simulations for this work were performed using USGS's Denali high-performance computer [82]. We acknowledge the efforts of Chris Sherwood, Jennifer Thomas, and Ben Norris for their valuable insight and peer review that improved the manuscript. Any use of trade, firm, or product names is for descriptive purposes only and does not imply endorsement by the U.S. Government.

Conflicts of Interest: The authors declare no conflict of interest.

Appendix A

Appendix A.1. Stream Discharge Multi-Linear Regression Gap-Filling

The daily mean fluvial discharge prescribed at the freshwater boundaries of the model was required to represent the Salish Sea density and its influence on regional coastal water levels. Historical stream discharge data are available from the U.S. Geological Survey (USGS) and Environment Canada for many but not all streams, and those with observations can contain gaps in temporal coverage. The stream discharge data needed for simulating the future were further limited to a few existing statistical or dynamic hydrologic models that downscale global climate model outputs of precipitation and effects on runoff (e.g., evapotranspiration).

The daily mean stream flow data for the period 1970–2020 from the USGS [69] and Environment Canada [70] for these purposes were gap-filled for missing data and seasonal variability through multilinear regressions of individual stream discharge data, Q_f, against other available stream discharge data, Q_i. The discharges were log-scaled to avoid negative discharge predictions and are related by:

$$\log Q_f = A + \sum_{i=1}^{N} (B_i \log Q_i)$$

where A and B_i are the regression coefficients. A second component was added to capture the strong seasonal signals in the discharge exhibited in different slopes for summer and winter utilizing another parameter, α, such that:

$$\log Q_f = A + \sum_{i=1}^{N} [\alpha_i B_i \log Q_i + (1 - \alpha_i) C_i log Q_i]$$

where

$$\alpha = \frac{1}{2} + \frac{1}{2} \cos[\frac{2\pi(t - \varnothing_i)}{365.25}]$$

with day of year, t, and seasonal offset, ϕ_i. The seasonal offset providing the best model fit was used. The non-parametric smearing correction described in reference [83] was implemented to remove bias introduced by the logarithmic transformation of discharge following:

$$Q_f^{corrected} = \frac{Q_f}{N} \sum_{i}^{N} e^{e_i}$$

where the residuals, e_i, are averaged for all observations, i.

The seasonal regression approach was applied in a multi-regression with all available stream data to each river with data gaps. The model skill varied, with resulting R^2 values ranging from 0.5 to 0.9 (Figure A1). Figure A2 compares the modeled and observed discharge results for six streams, representing a range of missing data and varied seasonal watershed drainage behavior. Lastly, the regression results were used to construct future time series stream discharge to the year 2100 based on the existing downscaled hydrological simulations for select streams provided in [76].

Appendix A.2. Meteorological Bias Correction

Numerical weather model wind forecasts including Weather Research and Forecasting (WRF) downscaled climate models [34] are coarser than many narrow waterways in the Salish Sea and Puget Sound. Where waterways are not resolved, wind speeds are typically biased low due to the higher friction parameterized over land in WRF simulations. To assess and correct this bias, 6 km WRF downscaled North American regional re-analysis [72] and 12-km WRF downscaled CMIP5 GFDL global climate model wind predictions [34] were compared with Canada's 2.5-km High-Resolution Deterministic Prediction System (HRDPS) forecasts over the period of available data from 2016 to 2020 [71].

The wind speed quantiles from HRDPS were compared to the 1985–2015 period of the re-analysis at each grid cell used for the hydrodynamic model. The same comparison was made for the 1970–2015 historical period of the CMIP5 GFDL model. The percent difference between the HRDPS and coarser model, for example, $\Delta U = (U_{HRDPS} - U_{GFDL})/U_{GFDL}$, in general, showed higher wind speeds over water, lower wind speeds over land, and greater differences at extremes, with the 99th percentiles showing differences up to 70%. We applied a correction factor, F_m, determined based on these differences, to the 6 km and 12 km WRF wind data, where $F_m = 1 + \Delta U$. Because extremes are the primary concern in coastal flood hazard estimation, the correction factor is an estimate with the 99th percentile comparison.

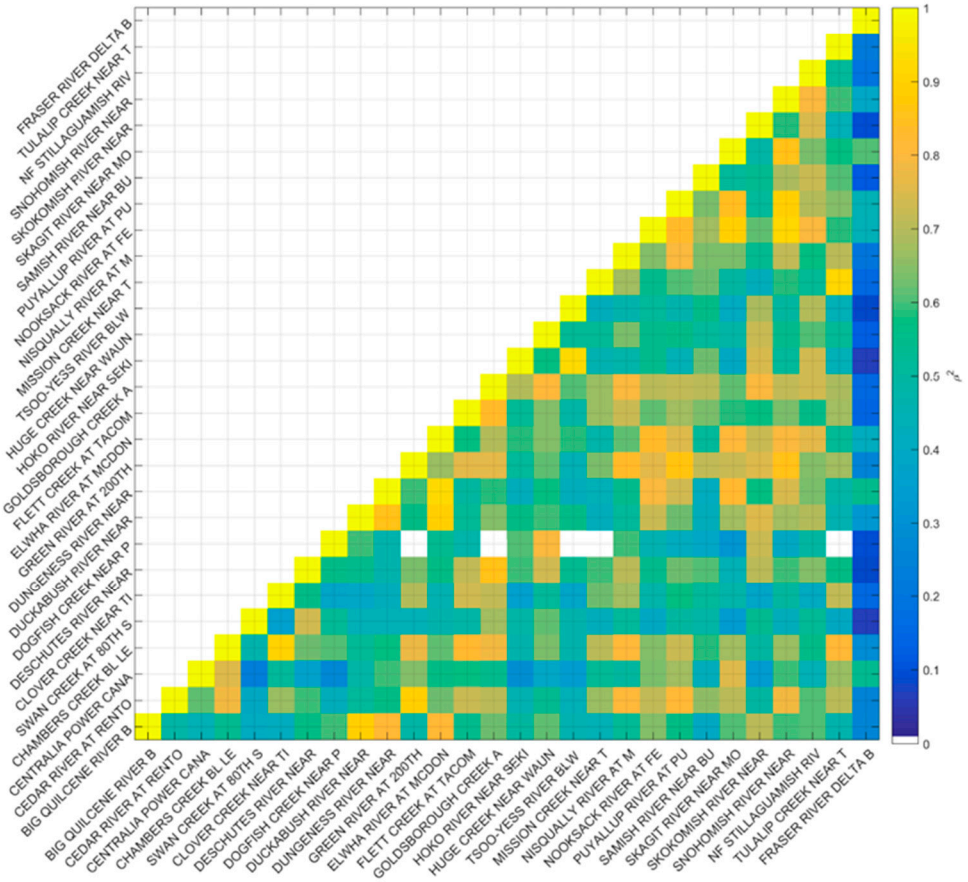


Figure A1. Correlation coefficient, rho^2, in color for each stream site combination on the x- and y-axes.

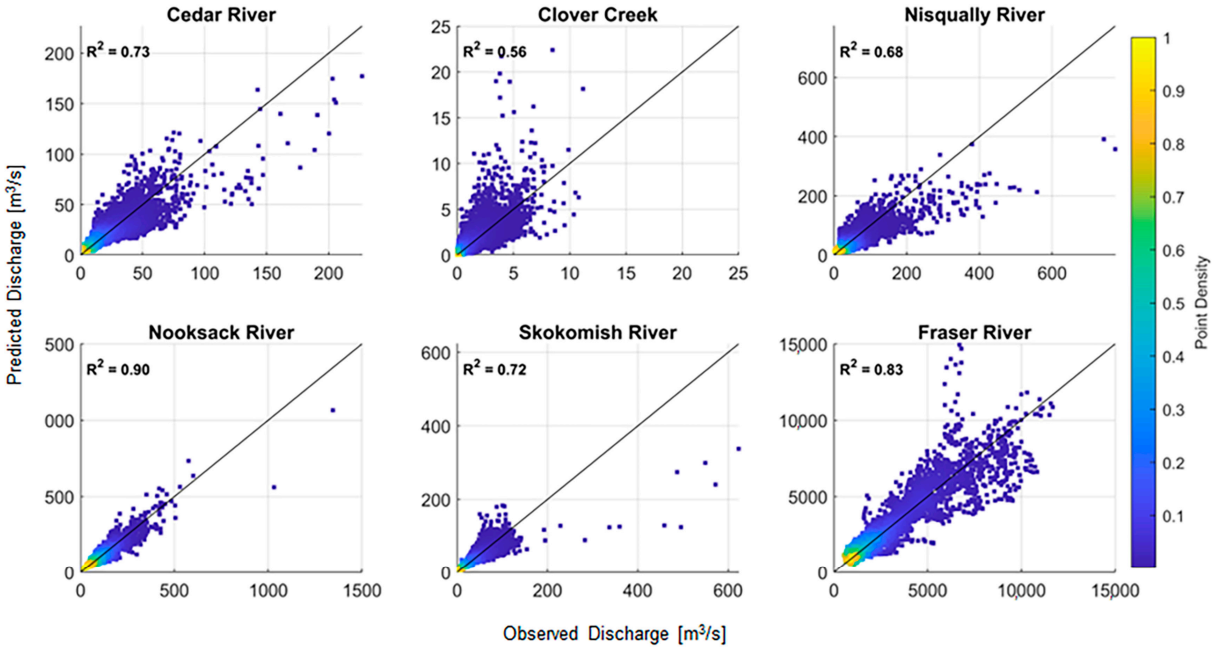


Figure A2. Predicted versus observed discharges for diverse streams in the region with point density in color (see colorbar) and coefficient of determination, R^2, at the upper left.

Though limited in their spatial coverage, local wind observations from available coastal NOAA meteorology stations [84] were also integrated into the calculated bias corrections. Similar to the model–model correction factors, observation–model correction factors, F_i,

using the 99th percentile at each observation location, i, were derived. We allowed the observations to influence the spatially varying correction factor, F, by defining a radius of spatial influence (stars in Figure A3). This radius, L_i, was determined subjectively based on the observation station proximity to land and wind speed variability, where in larger basins, L_i is larger, and in smaller basins, L_i is smaller (e.g., Port Townsend), see Table A1. The observation-adjusted correction factor, F, was then estimated as a combination of F_m and F_i. An exponential decay determined the averaging from the observation locations with a decay rate of $1/L_i$ written as follows:

$$F(x,y) = (1-w)F_m(x,y) + \sum_i w_i F_i$$

where

$$W_i = e^{-r_i(x,y)/L_i}$$

and r is the distance from x, y to the observation site in degrees. This correction factor, F, is estimated based on a 2.5 km grid and then applied to the 1985–2015 6 km re-analysis and 2015–2100 12-km future GDFL projected wind speeds (interpolated onto a 2.5 km grid) such that $U_{adj} = U_{gfdl} \times F$.

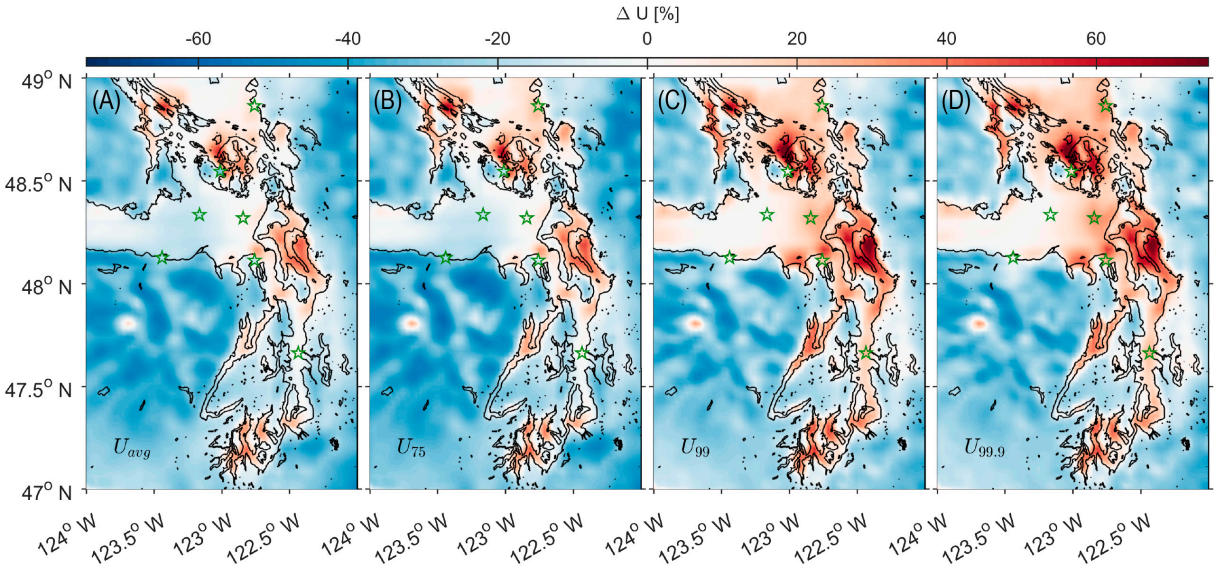


Figure A3. Percent differences between 12 km (GFDL) and 2.5 km (HRDPS) wind speeds for the mean (**A**), 75th (**B**), 90th (**C**), and 99th (**D**) percentiles (left to right). Green stars show similar percentiles estimated based on available meteorological observations.

Table A1. NOAA wind speed observation locations, Station ID, and decay length, L.

Name	ID	L
Hein Bank	46088	0.1
Port Townsend	PTWW1	0.01
Port Angeles	PTAW1	0.1
Friday Harbor	FRDW1	0.01
Smith Island	SISW1	0.1
West Point	WPOW1	0.15
Neah Bay	46087	0.01
Cherry Point	CHYW1	0.1

Note: Wind data sourced from [84].

References

1. Sweet, W.V.; Park, J. From the extreme to the mean: Acceleration and tipping points of coastal inundation from sea-level rise. *Earth's Future* **2014**, *2*, 579–600. [CrossRef]
2. Vitousek, S.; Barnard, P.L.; Fletcher, C.H.; Frazer, N.; Erikson, L.; Storlazzi, C.D. Doubling of coastal flooding frequency within decades due to sea-level rise. *Sci. Rep.* **2017**, *7*, 1399. [CrossRef] [PubMed]
3. Taherkhani, M.; Vitousek, S.; Barnard, P.L.; Frazer, N.; Anderson, T.R.; Fletcher, C.H. Sea-level rise exponentially increases coastal flood frequency. *Sci. Rep.* **2020**, *10*, 6466. [CrossRef] [PubMed]
4. Sweet, W.V.; Hamlington, B.D.; Kopp, R.E.; Weaver, C.P.; Barnard, P.L.; Bekaert, D.; Brooks, W.; Craghan, M.; Dusek, G.; Frederikse, T.; et al. *Global and Regional Sea Level Rise Scenarios for the United States: Updated Mean Projections and Extreme Water Level Probabilities Along U.S. Coastlines*; NOAA Technical Report NOS 01; National Oceanic and Atmospheric Administration, National Ocean Service: Silver Spring, MD, USA, 2022; 111p, Available online: https://oceanservice.noaa.gov/hazards/sealevelrise/noaa-nos-techrpt01-global-regional-SLR-scenarios-US.pdf (accessed on 15 February 2023).
5. Guérou, A.; Meyssignac, B.; Prandi, P.; Ablain, M.; Ribes, A.; Bignalet-Cazalet, F. Current Observed Global Mean Sea Level Rise and Acceleration Estimated from Satellite Altimetry and the Associated Uncertainty. *EGUsphere* **2022**, *19*, 431–451. [CrossRef]
6. Vermeer, M.; Rahmstorf, S. Global sea level linked to global temperature. *Proc. Natl. Acad. Sci. USA* **2009**, *106*, 21527–21532. [CrossRef] [PubMed]
7. Church, J.A.; White, N.J. Sea-Level Rise from the Late 19th to the Early 21st Century. *Surv. Geophys.* **2011**, *32*, 585–602. [CrossRef]
8. Leuliette, E.; Willis, J. Balancing the Sea Level Budget. *Oceanography* **2011**, *24*, 122–129. [CrossRef]
9. Hay, C.C.; Morrow, E.; Kopp, R.E.; Mitrovica, J.X. Probabilistic reanalysis of twentieth-century sea-level rise. *Nature* **2015**, *517*, 481–484. [CrossRef]
10. Barnard, P.L.; Erikson, L.H.; Foxgrover, A.C.; Hart, J.A.F.; Limber, P.; O'neill, A.C.; van Ormondt, M.; Vitousek, S.; Wood, N.; Hayden, M.K.; et al. Dynamic flood modeling essential to assess the coastal impacts of climate change. *Sci. Rep.* **2019**, *9*, 4309. [CrossRef]
11. Erikson, L.; Hegermiller, C.; Barnard, P.; Ruggiero, P.; van Ormondt, M. Projected wave conditions in the Eastern North Pacific under the influence of two CMIP5 climate scenarios. *Ocean Model.* **2015**, *96*, 171–185. [CrossRef]
12. Wahl, T.; Jain, S.; Bender, J.; Meyers, S.D.; Luther, M.E. Increasing risk of compound flooding from storm surge and rainfall for major US cities. *Nat. Clim. Chang.* **2015**, *5*, 1093–1097. [CrossRef]
13. Zscheischler, J.; Westra, S.; Van Den Hurk, B.J.J.M.; Seneviratne, S.I.; Ward, P.J.; Pitman, A.; AghaKouchak, A.; Bresch, D.N.; Leonard, M.; Wahl, T.; et al. Future climate risk from compound events. *Nat. Clim. Chang.* **2018**, *8*, 469–477. [CrossRef]
14. Bromirski, P.D.; Miller, A.J.; Flick, R.E.; Auad, G. Dynamical suppression of sea level rise along the Pacific coast of North America: Indications for imminent acceleration. *J. Geophys. Res. Atmos.* **2011**, *116*, C07005. [CrossRef]
15. Tehranirad, B.; Herdman, L.; Nederhoff, K.; Erikson, L.; Cifelli, R.; Pratt, G.; Leon, M.; Barnard, P. Effect of Fluvial Discharges and Remote Non-Tidal Residuals on Compound Flood Forecasting in San Francisco Bay. *Water* **2020**, *12*, 2481. [CrossRef]
16. Nederhoff, K.; Saleh, R.; Tehranirad, B.; Herdman, L.; Erikson, L.; Barnard, P.L.; Van der Wegen, M. Drivers of extreme water levels in a large, urban, high-energy coastal estuary–a case study of the san francisco bay. *Coast. Eng.* **2021**, *170*, 103984. [CrossRef]
17. Morey, S.L.; Baig, S.; Bourassa, M.A.; Dukhovskoy, D.S.; O'Brien, J.J. Remote forcing contribution to storm-induced sea level rise during Hurricane Dennis. *Geophys. Res. Lett.* **2006**, *33*, L19603. [CrossRef]
18. Zhong, L.; Li, M.; Zhang, D.L. How do uncertainties in hurricane model forecasts affect storm surge predictions in a semi-enclosed bay? *Estuar. Coast Shelf Sci.* **2010**, *90*, 61–72. [CrossRef]
19. Liu, X.; Jiang, W.; Yang, B.; Baugh, J. Numerical study on factors influencing typhoon-induced storm surge distribution in Zhanjiang Harbor. *Estuar. Coast Shelf Sci.* **2018**, *215*, 39–51. [CrossRef]
20. Durski, S.M.; Kurapov, A.L.; Allen, J.S.; Kosro, P.M.; Egbert, G.D.; Shearman, R.K.; Barth, J.A. Coastal ocean variability in the US Pacific Northwest region: Seasonal patterns, winter circulation, and the influence of the 2009–2010 El Niño. *Ocean Dyn.* **2015**, *65*, 1643–1663. [CrossRef]
21. Hamlington, B.D.; Leben, R.R.; Kim, K.; Nerem, R.S.; Atkinson, L.P.; Thompson, P.R. The effect of the El Niño-Southern Oscillation on U.S. regional and coastal sea level. *J. Geophys. Res. Oceans* **2015**, *120*, 3970–3986. [CrossRef]
22. Kurapov, A.; Pelland, N.; Rudnick, D. Seasonal and interannual variability in along-slope oceanic properties off the us west coast: Inferences from a high-resolution regional model. *J. Geophys. Res. Oceans* **2017**, *122*, 5237–5259. [CrossRef]
23. MacMahan, J. Observations of oceanic-forced subtidal elevations in a convergent estuary. *Estuar. Coast Shelf Sci.* **2016**, *181*, 319–324. [CrossRef]
24. Murty, T.; Venkatesh, S.; Danard, M.; El-Sabh, M. Storm surges in Canadian waters. *Atmosphere-Ocean* **1995**, *33*, 359–387. [CrossRef]
25. Thompson, P.R.; Merrifield, M.A.; Wells, J.R.; Chang, C.M. Wind-Driven Coastal Sea Level Variability in the Northeast Pacific. *J. Clim.* **2014**, *27*, 4733–4751. [CrossRef]
26. Barnard, P.L.; Short, A.D.; Harley, M.D.; Splinter, K.D.; Vitousek, S.; Turner, I.L.; Allan, J.; Banno, M.; Bryan, K.R.; Doria, A.; et al. Coastal vulnerability across the Pacific dominated by El Niño/Southern Oscillation. *Nat. Geosci.* **2015**, *8*, 801–807. [CrossRef]
27. Barnard, P.L.; Hoover, D.; Hubbard, D.M.; Snyder, A.; Ludka, B.C.; Allan, J.; Kaminsky, G.M.; Ruggiero, P.; Gallien, T.W.; Gabel, L.; et al. Extreme oceanographic forcing and coastal response due to the 2015–2016 El Niño. *Nat. Commun.* **2017**, *8*, 14365. [CrossRef]
28. Flick, R.E. California tides, sea level, and waves—Winter 2015–2016. *Shore Beach* **2016**, *84*, 25–30.

29. Soontiens, N.; Allen, S.E.; Latornell, D.; Le Souëf, K.; Machuca, I.; Paquin, J.-P.; Lu, Y.; Thompson, K.; Korabel, V. Storm Surges in the Strait of Georgia Simulated with a Regional Model. *Atmosphere-Ocean* **2015**, *54*, 1–21. [CrossRef]
30. Vos, K.; Harley, M.D.; Turner, I.L.; Splinter, K.D. Pacific shoreline erosion and accretion patterns controlled by El Niño/Southern Oscillation. *Nat. Geosci.* **2023**, *16*, 140–146. [CrossRef]
31. Muis, S.; Apecechea, M.I.; Dullaart, J.; Rego, J.d.L.; Madsen, K.S.; Su, J.; Yan, K.; Verlaan, M. A High-Resolution Global Dataset of Extreme Sea Levels, Tides, and Storm Surges, Including Future Projections. *Front. Mar. Sci.* **2020**, *7*, 263. [CrossRef]
32. Chassignet, E.P.; Hurlburt, H.E.; Smedstad, O.M.; Halliwell, G.R.; Hogan, P.J.; Wallcraft, A.J.; Baraille, R.; Bleck, R. The HYCOM (HYbrid Coordinate Ocean Model) data assimilative system. *J. Mar. Syst.* **2007**, *65*, 60–83. [CrossRef]
33. Yang, Z.; Wang, T.; Castrucci, L. Storm Surge Modeling in Puget Sound. Technical Report. Pacific Northwest National Lab (PNNL), Richland, WA (United States). 2019. Available online: https://www.osti.gov/servlets/purl/1558622 (accessed on 15 May 2020).
34. Mass, C.F.; Salath'e Jr, E.P.; Steed, R.; Baars, J. The mesoscale response to global warming over the pacific northwest evaluated using a regional climate model ensemble. *J. Clim.* **2022**, *35*, 2035–2053. [CrossRef]
35. Sobocinski, K.L. State of the Salish Sea. G. Broadhurst and N.J.K. Baloy (Contributing Eds.). Salish Sea Institute, Western Washington University. 2021. Available online: https://cedar.wwu.edu/salish_pubs/1/ (accessed on 1 February 2022).
36. Steenburgh, W.J.; Mass, C.F. Interaction of an Intense Extratropical Cyclone with Coastal Orography. *Mon. Weather Rev.* **1996**, *124*, 1329–1352. [CrossRef]
37. Martin, J.E.; Grauman, R.D.; Marsili, N. Surface Cyclolysis in the North Pacific Ocean. Part I: A Synoptic Climatology. *Mon. Weather Rev.* **2001**, *129*, 748–765. [CrossRef]
38. Eichler, T.; Higgins, W. Climatology and ENSO-Related Variability of North American Extratropical Cyclone Activity. *J. Clim.* **2006**, *19*, 2076–2093. [CrossRef]
39. Abeysirigunawardena, D.S.; Gilleland, E.; Bronaugh, D.; Wong, P. Extreme wind regime responses to climate variability and change in the inner south coast of British Columbia, Canada. *Atmosphere-Ocean* **2009**, *47*, 41–62. [CrossRef]
40. Grossman, E.; Stevens, A.; Dartnell, P.; George, D.; Finlayson, D. Sediment export and impacts associated with river delta channelization compound estuary vulnerability to sea-level rise, Skagit River Delta, Washington, USA. *Mar. Geol.* **2020**, *430*, 106336. [CrossRef]
41. Hanna, J.M. *Native Communities and Climate Change: Protecting Tribal Resources as Part of National Climate Policy*; Natural Resources Law Center, University of Colorado Law School: Boulder, CO, USA, 1997.
42. Status of Tribes and Climate Change Working Group. *Status of Tribes and Climate Change Report*; Marks-Marino, D., Ed.; Institute for Tribal Environmental Professionals, Northern Arizona University: Flagstaff, AZ, USA, 2021; Available online: http://nau.edu/stacc%202021 (accessed on 22 November 2023).
43. Mofjeld, H.O.; Larsen, L.H. *Tides and Tidal Currents of the Inland Waters of Western Washington*; NOAA Technical Memorandum ERL PMEL-56; National Oceanic and Atmospheric Administration: Washington, DC, USA, 1984.
44. Lavelle, J.W.; Cokelet, E.D.; Cannon, G.A. A model study of density intrusions into and circulation within a deep, silled estuary: Puget Sound. *J. Geophys. Res. Atmos.* **1991**, *96*, 16779. [CrossRef]
45. Babson, A.L.; Kawase, M.; MacCready, P. Seasonal and Interannual Variability in the Circulation of Puget Sound, Washington: A Box Model Study. *Atmosphere-Ocean* **2006**, *44*, 29–45. [CrossRef]
46. Yang, Z.; Khangaonkar, T. Multi-scale modeling of Puget Sound using an unstructured-grid coastal ocean model: From tide flats to estuaries and coastal waters. *Ocean Dyn.* **2010**, *60*, 1621–1637. [CrossRef]
47. Sutherland, D.A.; MacCready, P.; Banas, N.S.; Smedstad, L.F. A Model Study of the Salish Sea Estuarine Circulation. *J. Phys. Oceanogr.* **2011**, *41*, 1125–1143. [CrossRef]
48. Abeysirigunawardena, D.S.; Smith, D.J.; Taylor, B. Extreme Sea Surge Responses to Climate Variability in Coastal British Columbia, Canada. *Ann. Assoc. Am. Geogr.* **2011**, *101*, 992–1010. [CrossRef]
49. Yang, Z.; Wang, T. Tidal residual eddies and their effect on water exchange in Puget Sound. *Ocean Dyn.* **2013**, *63*, 995–1009. [CrossRef]
50. Yang, Z.; Wang, T.; Leung, R.; Hibbard, K.; Janetos, T.; Kraucunas, I.; Rice, J.; Preston, B.; Wilbanks, T. A modeling study of coastal inundation induced by storm surge, sea-level rise, and subsidence in the Gulf of Mexico. *Nat. Hazards* **2013**, *71*, 1771–1794. [CrossRef]
51. Yang, Z.; Wang, T.; Voisin, N.; Copping, A. Estuarine response to river flow and sea-level rise under future climate change and human development. *Estuar. Coast Shelf Sci.* **2015**, *156*, 19–30. [CrossRef]
52. Khangaonkar, T.; Long, W.; Xu, W. Assessment of circulation and inter-basin transport in the Salish Sea including Johnstone Strait and Discovery Islands pathways. *Ocean Model.* **2017**, *109*, 11–32. [CrossRef]
53. Miller, I.M.; Morgan, H.; Mauger, G.; Newton, T.; Weldon, R.; Schmidt, D.; Welch, M.; Grossman, E.E. Projected Sea Level Rise for Washington State—A 2018 Assessment: Prepared for the Washington Coastal Resilience Project. 2018. 24p. Available online: http://www.wacoastalnetwork.com/files/theme/wcrp/SLR-Report-Miller-et-al-2018.pdf (accessed on 22 November 2023).
54. Yang, Z.; Wang, T.; Castrucci, L.; Miller, I. Modeling assessment of storm surge in the Salish Sea. *Estuar. Coast Shelf Sci.* **2019**, *238*, 106552. [CrossRef]

55. Bromirski, P.D.; Flick, R.E.; Miller, A.J. Storm surge along the Pacific coast of North America. *J. Geophys. Res. Oceans* **2017**, *122*, 441–457. [CrossRef]
56. Kernkamp, H.W.; Van Dam, A.; Stelling, G.S.; de Goede, E.D. Efficient scheme for the shallow water equations on unstructured grids with application to the continental shelf. *Ocean Dyn.* **2011**, *61*, 1175–1188. [CrossRef]
57. Tyler, D.J.; Danielson, J.J.; Grossman, E.E.; Hockenberry, R.J. Topobathymetric Model of the Strait of Juan de Fuca, 1891 to 2016: U.S. Geological Survey Data Release. 2021. Available online: https://www.sciencebase.gov/catalog/item/5d7641bee4b0c4f70d01f564 (accessed on 22 November 2023).
58. Tyler, D.J.; Danielson, J.J.; Grossman, E.E.; Hockenberry, R.J. *Topobathymetric Model of Puget Sound, Washington, 1887 to 2017*; U.S. Geological Survey: Reston, VA, USA, 2020. [CrossRef]
59. Carignan, K.; Eakins, B.; Love, M.; Sutherland, M.; McLean, S. Bathymetric Digital Elevation Model of British Columbia, Canada: Procedures, Data Sources, and Analysis. NOAA National Geophysical Data Center (NGDC). 2013. Available online: https://www.ncei.noaa.gov/access/metadata/landing-page/bin/iso?id=gov.noaa.ngdc.mgg.dem:4956 (accessed on 15 May 2019).
60. NOAA; NOAA National Geophysical Data Center. Strait of Juan de Fuca 36 arc-second MHW Coastal Digital Elevation Model. NOAA National Centers for Environmental Information: USA, 2013.
61. Sternberg, R. Friction factors in tidal channels with differing bed roughness. *Mar. Geol.* **1968**, *6*, 243–260. [CrossRef]
62. Grossman, E.E.; Tehranirad, B.; Stevens, A.W.; VanArendonk, N.R.; Crosby, S.; Nederhoff, K. *Salish Sea Hydrodynamic Model: U.S. Geological Survey Data Release*; U.S. Geological Survey: Reston, VA, USA, 2023. [CrossRef]
63. Lyard, F.; Lefevre, F.; Letellier, T.; Francis, O. Modelling the global ocean tides: Modern insights from FES2004. *Ocean Dyn.* **2006**, *56*, 394–415. [CrossRef]
64. Holbrook, J. *Circulation in the Strait of Juan de Fuca: Recent Oceanographic Observations in the Eastern Basin*; US Department of Commerce, National Oceanic and Atmospheric Administration: Washington, DC, USA, 1980; Volume 55. Available online: https://repository.library.noaa.gov/view/noaa/17346 (accessed on 15 May 2019).
65. Moore, S.K.; Mantua, N.J.; Newton, J.A.; Kawase, M.; Warner, M.J.; Kellogg, J.P. A descriptive analysis of temporal and spatial patterns of variability in Puget Sound oceanographic properties. *Estuar. Coast Shelf Sci.* **2008**, *80*, 545–554. [CrossRef]
66. Washington Department of Ecology. Environmental Information Management System. 2022. Available online: http://www.ecology.wa.gov/eim/ (accessed on 22 November 2023).
67. Fofonoff, N.P. Physical properties of seawater: A new salinity scale and equation of state for seawater. *J. Geophys. Res. Ocean.* **1985**, *90*, 3332–3342. [CrossRef]
68. Czuba, J.A.; Magirl, C.S.; Czuba, C.R.; Grossman, E.E.; Curran, C.A.; Gendaszek, A.S.; Dinicola, R.S. *Sediment Load from Major Rivers into Puget Sound Its Adjacent Waters*; Fact Sheet 2011–3083; U.S. Geological Survey: Reston, VA, USA, 2011; 4p. Available online: http://pubs.usgs.gov/fs/2011/3083/ (accessed on 22 November 2023).
69. US Geological Survey [USGS]. National Water Information System: U.S. Geological Survey Website. 2022. Available online: https://nwis.waterdata.usgs.gov/nwis (accessed on 1 May 2023). [CrossRef]
70. Environment and Natural Resources Canada. 2020. Available online: https://wateroffice.ec.gc.ca/ (accessed on 1 July 2021).
71. Environment Canada. 2020. Available online: https://weather.gc.ca/ (accessed on 2 February 2021).
72. Chen, X.; Leung, L.R.; Gao, Y.; Liu, Y.; Wigmosta, M.; Richmond, M. Predictability of Extreme Precipitation in Western U.S. Watersheds Based on Atmospheric River Occurrence, Intensity, and Duration. *Geophys. Res. Lett.* **2018**, *45*, 11693–11701. [CrossRef]
73. Mesinger, F.; DiMego, G.; Kalnay, E.; Mitchell, K.; Shafran, P.C.; Ebisuzaki, W.; Jović, D.; Woollen, J.; Rogers, E.; Berbery, E.H.; et al. North American Regional Reanalysis. *Bull. Am. Meteorol. Soc.* **2006**, *87*, 343–360. [CrossRef]
74. Nowacki, D.J.; Stevens, A.W.; Vanarendonk, N.R.; Grossman, E.E. *Time-Series Measurements of Pressure, Conductivity, Temperature, and Water Level Collected in Puget Sound and Bellingham Bay, Washington, USA, 2018 to 2021*; U.S. Geological Survey Data Release; U.S. Geological Survey: Reston, VA, USA, 2021. [CrossRef]
75. Codiga, D.L. Unified tidal Analysis and Prediction Using the Utide Matlab Functions. 2011. Available online: https://www.mathworks.com/matlabcentral/fileexchange/46523-utide-unified-tidal-analysis-and-prediction-functions (accessed on 22 November 2023).
76. Hamlet, A.F.; Elsner, M.M.; Mauger, G.S.; Lee, S.-Y.; Tohver, I.; Norheim, R.A. An Overview of the Columbia Basin Climate Change Scenarios Project: Approach, Methods, and Summary of Key Results. *Atmosphere-Ocean* **2013**, *51*, 392–415. [CrossRef]
77. Coles, S.; Bawa, J.; Trenner, L.; Dorazio, P. *An Introduction to Statistical Modeling of Extreme Values*; Springer: Berlin/Heidelberg, Germany, 2001; Volume 208.
78. Folland, C.K.; Parker, D. Correction of instrumental biases in historical sea surface temperature data. *Q. J. R. Meteorol. Soc.* **1995**, *121*, 319–367. [CrossRef]
79. Ishii, M.; Shouji, A.; Sugimoto, S.; Matsumoto, T. Objective analyses of sea-surface temperature and marine meteorological variables for the 20th century using ICOADS and the Kobe Collection. *Int. J. Clim.* **2005**, *25*, 865–879. [CrossRef]
80. Stronach, J.A.; Backhaus, J.O.; Murty, T.S. An update on the numerical simulation of oceanographic processes in the waters between vancouver island and the mainland: The gf8 model. *Oceanogr. Mar. Biol. Annu. Rev.* **1993**, *31*, 1–86.
81. Foreman, M.; Sutherland, G.; Cummins, P. M2 tidal dissipation around Vancouver Island: An inverse approach. *Cont. Shelf Res.* **2004**, *24*, 2167–2185. [CrossRef]

82. Falgout, J.T.; Gordon, J.; Williams, B.; Davis, M.J. *USGS Advanced Research Computing USGS Denali Supercomputer*; U.S. Geological Survey: Reston, VA, USA, 2023. [CrossRef]
83. Duan, N. Smearing Estimate: A Nonparametric Retransformation Method. *J. Am. Stat. Assoc.* **1983**, *78*, 605. [CrossRef]
84. NOAA Climate Data Online. 2020. Available online: https://www.ncei.noaa.gov/cdo-web/ (accessed on 30 June 2020).

Disclaimer/Publisher's Note: The statements, opinions and data contained in all publications are solely those of the individual author(s) and contributor(s) and not of MDPI and/or the editor(s). MDPI and/or the editor(s) disclaim responsibility for any injury to people or property resulting from any ideas, methods, instructions or products referred to in the content.